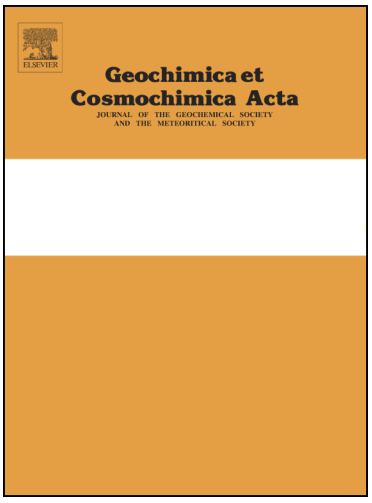

Platinum Group Element Geochemistry of the Forest Reef Volcanics, South-eastern Australia: Implications for Porphyry Au-Cu Mineralisation

Jessica N. Lowczak, Ian H. Campbell, Helen Cocker, Jung-Woo Park, David R. Cooke

PII: S0016-7037(17)30641-5
DOI: https://doi.org/10.1016/j.gca.2017.09.052
Reference: GCA 10504

To appear in: *Geochimica et Cosmochimica Acta*

Received Date: 26 November 2016
Accepted Date: 30 September 2017

Please cite this article as: Lowczak, J.N., Campbell, I.H., Cocker, H., Park, J-W., Cooke, D.R., Platinum Group Element Geochemistry of the Forest Reef Volcanics, Southeastern Australia: Implications for Porphyry Au-Cu Mineralisation, *Geochimica et Cosmochimica Acta* (2017), doi: https://doi.org/10.1016/j.gca.2017.09.052

Platinum Group Element Geochemistry of the Forest Reef Volcanics, Southeastern Australia: Implications for Porphyry Au-Cu Mineralisation

Jessica N. Lowczak[1*], Ian H. Campbell[1], Helen Cocker[1], Jung-Woo Park[1,2], David R. Cooke[3]

[1]*Research School of Earth Sciences, Australian National University, Australian Capital Territory 0200, Australia*

[2]*School of Earth and Environmental Sciences and Research Institute of Oceanography, Seoul National University, Seoul 08826, South Korea*

[3]*CODES ARC Centre of Excellence in Ore Deposits, University of Tasmania, Private Bag 126, Hobart, Tasmania 7001, Australia*

* Corresponding author: e-mail, Jessica.lowczak@anu.edu.au

Abstract

Platinum group element concentrations in felsic to intermediate rocks from the Forest Reef Volcanics, Cadia-Neville region, southeastern Australia have been analysed by the Ni-S fire assay-isotope dilution method. The Forest Reef Volcanics are shoshonitic to calc-alkaline in composition and fractionated to produce a wide range of compositions, with MgO varying between 9.7 and 1.8 wt.%. The interest in this suite is that it is coeval with Au-Cu porphyry-style mineralisation in the Cadia mineral district. This study uses PGE geochemistry to determine the timing of sulfide saturation, relative to volatile (ore-fluid) saturation, in the magma that gave rise to the Forest Reef Volcanics and, in turn, to assess how this timing affected the mineralisation potential of the evolving magmatic system.

The Forest Reef Volcanics can be subdivided, on the basis of their contrasting PGE geochemistry, into high-Mg (>6.8 wt.% MgO) and low-Mg suites (≤6.8 wt.% MgO). Platinum, Pd and Re concentrations increase in the high-Mg samples, whereas Ir and Ru decrease and Rh concentrations remain steady, with decreasing MgO. The coupled Ir, Ru and Rh depletion is attributed to the partitioning of these elements into magnetite. The rate of Pt and Pd enrichment is not possible by closed-system fractional crystallisation alone, which suggests that the parent magma was replenished by a Pt-Pd-rich melt. In contrast, the PGE concentrations in the low-Mg samples decrease with decreasing MgO indicating the onset of sulfide saturation at 6.8 wt.% MgO, which is confirmed by the presence of spheroidal sulfide inclusions in liquidus crystals (i.e. clinopyroxene, plagioclase, magnetite). The rate of Pd depletion is appreciably less than for any other sulfide saturated felsic system for which data are available. This requires either that the amount of sulfide melt to have precipitated was unusually low, or that the rate of Pd depletion was limited by the mass of silicate melt the sulfide melt reached equilibrium with, or both. In any event, the fraction of sulfide melt that precipitated was too small to have had a significant affect on the Cu and Au content of the magma so that both Cu and Au were available to enter the ore-forming fluid when the magma became volatile saturated at, or shortly after, it reached ca. 2.9 wt.% MgO.

1. Introduction

Platinum-group elements (PGE; Os, Ir, Ru, Rh, Pt, Pd) are highly chalcophile and can be used to constrain the role of sulfides in magmatic processes, including mantle petrogenesis, magmatic differentiation and the timing of sulfide saturation (Naldrett and Duke, 1980). The PGE geochemistry of ultra-mafic to mafic systems has been studied extensively because of their association with economic Ni-Cu-PGE deposits (e.g. Noril'sk, Siberia; Jinchuan, China; Voisey's Bay, Canada; Kambalda, Australia; Naldrett, 1999). Studies on PGE in felsic to intermediate systems, such as those associated with porphyry Au-Cu deposits, have been limited due to the difficulty of measuring PGE at the ultra-low concentrations (sub-ng/g- to pg/g-level) at which they are present in these systems (Park et al., 2013a). However, a recent refinement of the Ni-S fire assay-isotope dilution method at the Australian National University (ANU) allows the determination of the PGE at the pg/g-level.

Processes that contribute to the formation of economic porphyry-style mineralisation include: (i) those that influence metal endowment during magma generation, (ii) magma chamber processes that enrich or deplete the magma in Cu and Au during fractional crystallisation, and (iii) magmatic-hydrothermal processes that mobilise metals from the magma chamber to the site of Au-Cu or Cu mineralisation. Although all three processes are important, the focus of this study is on process (ii): the contribution of magmatic processes to ore formation.

The significance of the PGE is that their extreme partition coefficients make them sensitive indicators of sulfide saturation (Park et al., 2013b). The aim of this study was to test the hypothesis that the timing of sulfide saturation relative to volatile saturation controls the fertility of an evolving felsic system and, in the case of a fertile system, whether the ore that forms is Au-Cu or Cu-only. If sulfide saturation occurs before volatile saturation the sulfide melt will sequester Cu, Au and PGE from the silicate melt and lock these elements in disseminated sulfide phases in a deep underlying magma chamber, where they are unavailable to enter magmatic-hydrothermal fluids (Park et al., 2013b). Conversely, if volatile saturation occurs before sulfide saturation, Cu, Au and the PGE will be available to enter a magmatic-hydrothermal fluid, which may produce Cu-only or Au-Cu mineralisation. The term 'volatile phase', as used in this study,

encompasses H_2O-rich vapour or brine but does not include CO_2 gas, which saturates early from an evolving magma (Lowenstern, 2001) but has negligible effect on the PGE-Au-Cu budget.

The PGE are used in preference to Cu and Au to identify the timing of sulfide saturation for two reasons. First, because PGE partition more strongly into a sulfide melt than Cu or Au (e.g. Mungall and Brenan, 2014) and are therefore more sensitive indicators of sulfide saturation. Second, the PGE are significantly less mobile than Cu or Au in hydrothermal fluids and, as a result, their concentrations in rocks are dominated by magmatic rather than hydrothermal processes (e.g. Mukherjee et al., 2014; Park et al., 2016).

The aim of this study was to measure the ultra-low PGE concentrations in the Forest Reef Volcanics, from the Cadia-Neville Region in southeastern Australia, to constrain the timing of sulfide saturation relative to volatile saturation in the magma that gave rise to this suite (Fig. 1). The Forest Reef Volcanics are of interest because of their genetic association with Au-Cu porphyry-style mineralisation in the Cadia mineral district. This study will improve the understanding of felsic magmatic processes, and in particular, the timing of sulfide saturation, and how this affects the mineralisation potential of the magmatic system. Sulfide saturation occurred early in the Forest Reef Volcanics, well before volatile saturation. However, the low rate of PGE depletion with fractionation indicates that the amount of sulfide melt to have precipitated was too small to affect the net concentrations of Cu and Au in the evolved silicate melt. As a consequence, the magma that gave rise to the ore-associated intrusions at Cadia, which are thought to be the plutonic expression of the Forest Reef Volcanics (Harris et al., 2014), was not depleted in Au or Cu at the time of volatile saturation and therefore able to form an economic Au-Cu deposit.

1.1 Geological background

The Lachlan Fold Belt preserves a complex subduction-accretionary history spanning the Cambrian to Carboniferous with the most significant event being the collision of Gondwanaland's proto-Pacific margin with an oceanic terrane, the Macquarie Arc, during the Late Ordovician (ca. 455–448 Ma; Squire and Crawford, 2007). This collision resulted in regional uplift, the closure of

a back-arc basin and a quiescent period with little arc-magmatism (Glen et al., 1998). Shortly thereafter (ca. 440 Ma), east–directed slab roll–back resulted in extensional rifting (Crawford, 2007). The development of deep–seated extension along the Lachlan Transverse Zone (LTZ) is interpreted to have triggered decompressional partial melting of a subduction-modified mantle and facilitated the emplacement of high-K calc-alkaline and shoshonitic magmas, including the Forest Reef Volcanics, to higher crustal levels in a volcano-sedimentary sub-basin (Fox et al., 2015).

The Lachlan Fold Belt is host to a range of magmatic-hydrothermal deposits including porphyry Au-Cu, Fe-Cu skarn, high–sulfidation Au and carbonate base–metal epithermal deposits, with porphyry mineralisation being the most economically significant (Cooke et al., 2007). All four deposit styles are hosted either within the Cadia or Northparkes mineral districts, and are genetically associated with the high-K, calc-alkaline to shoshonitic magmas emplaced in a volcano-sedimentary sub-basin during the Late Ordovician to Early Silurian. The largest Au-Cu deposit in the region, Cadia East, contains >37 MOz (>1.05 x 10^6 kg) of Au, which is hosted in quartz-calcite-sulfide veins that strike parallel to alkali porphyry dikes (Fox et al., 2015). Two discrete mineralising events occurred at Cadia, with the first at ca. 460–450 Ma, and second at ca. 443–439 Ma (Wilson et al., 2007).

The Forest Reef Volcanics encompass both porphyritic intrusive (monzonite, syenite) and volcanic (basalt, andesite, latite) rocks (Harris et al., 2014; Fox et al., 2015). Units of the Forest Reef Volcanics represent the upper sequences of the volcano-sedimentary sub-basin, and are host to younger alkali-porphyry dikes, and associated Au-Cu mineralisation. The Forest Reef Volcanics were deposited during the Middle to Late Ordovician (Harris et al., 2014; Fox et al., 2015) and intruded by alkali porphyry dikes (Cadia Intrusive Complex), that gave rise to Au-Cu mineralisation, shortly thereafter during the Early Silurian (ca. 440 to 437 Ma; Squire and Crawford, 2007; Wilson et al., 2007).

The Forest Reef Volcanics show temporal variation in their geochemistry from shoshonitic (ca. 463–453 Ma) to medium-K calc-alkaline (ca. 448–445 Ma) and back to high–K calc-alkaline and

shoshonitic magmatism (ca. 443–439 Ma; Squire and Crawford, 2007). The focus of this study is on the volcanic and intrusive rocks from the latter period (ca. 443–439 Ma). Samples used in this study vary in composition from trachyandesites and trachydacites through to basalts, basaltic trachyandesites, syenites and porphyritic monzonites (Squire and Crawford, 2007).

The magmas from which the intrusive and volcanic rocks in the Cadia-Neville region crystallised were strongly oxidised (Blevin, 2002). They have high εNd values, with the Forest Reef Volcanics ranging from εNd +6.2 to +6.9 (Squire and Crawford, 2007), which closely resemble values of the Ordovician depleted upper mantle (εNd +5.7 to 8.0; Wyborn and Sun, 1993) and, in combination with low $^{87}Sr/^{86}Sr$ ratios (0.704; Cooke et al., 2007), indicate a primitive mantle source with negligible crustal assimilation (Squire and Crawford, 2007).

1.2 Petrography of the Forest Reef Volcanics

A detailed petrographic description of samples used in this study, as previously described by Squire (2001), is provided in supplementary information, Table A.1. The following is a brief overview of each unit as described by Squire (2001).

Burnt Yards Basalt and *Sundew Basalt*

Highly porphyritic basalt to basaltic andesite comprised of euhedral to subhedral, fine- to medium-grained (0.3-5.0 mm) clinopyroxene (20-40%), plagioclase (15-35%), olivine (0-2%) with trace amounts of FeTi-oxide set in a fine- to medium-grained holocrystalline quartzofeldspathic groundmass containing minor clinopyroxene, FeTi-oxides and opaques.

Porphyritic Nullawonga Latite Member

Highly porphyritic trachyandesite containing weak to moderate flow foliation. The samples consist of euhedral to subhedral, fine- to medium-grained (0.3-5.0 mm) plagioclase (25-40%), clinopyroxene (3-5%), biotite (3%), and K-feldspar (2%) crystals with trace amounts of FeTi-oxide and up to 20% volcanic clasts set in a fine- to medium-grained holocrystalline plagioclase, and minor clinopyroxene, groundmass.

Glen Ayre Syenite

Holocrystalline syenite comprised of euhedral to subhedral, fine- to medium-grained (0.3-4.0 mm) plagioclase (35-50%), K-feldspar (35-60%), clinopyroxene (5-25%), biotite (10%) and apatite (1%) crystals, poikilitically enclosed by K-feldspar.

Errowan Intrusive Complex

Highly porphyritic monzonite comprised of variable amounts of equigranular, euhedral to subhedral, fine- to medium-grained (0.4-7.0 mm) plagioclase (20-60%), clinopyroxene (7-30%), hornblende (0-25%), K-feldspar (10-30%), biotite (0-2%), and quartz (0-10%) with trace amounts of apatite and FeTi-oxide, set in a fine-grained holocrystalline quartzo-feldspathic groundmass.

Hornblende Basalt Andesite Intrusion

Highly porphyritic basaltic andesite comprised of euhedral to subhedral, fine-to medium-grained (0.3-5.0 mm) plagioclase (10-50%), clinopyroxene (7-15%) and hornblende (5-20%) with traces of apatite and FeTi-oxides, set in a fine- to medium-grained holocrystalline quartzo-feldspathic groundmass.

The Forest Reef Volcanics are closely spatially and temporally associated with porphyry Au-Cu mineralisation. As a consequence, samples have been subjected to varying degrees of potassic, propylitic or quartz-albite alteration (Holliday et al., 2002). This alteration is commonly observed as partial- to complete-replacement of primary plagioclase by calcite, sericite and/or albite; clinopyroxene by actinolite, chlorite and/or epidote; and olivine by chlorite and/or actinolite (supplementary information, Table A.1). A few samples contain additional secondary (hydrothermal) sulfides, notably pyrite with minor chalcopyrite. The total amount of secondary sulfides does not exceed 1% modal of the bulk rock.

This study concentrates on 13 of the least altered volcanic and intrusive rocks. Least-altered samples were determined by petrographic examination of all available samples in thin section (28 samples). Samples containing the least amount of secondary minerals, including sulfides, and

least destruction of primary mineral textures, were selected. Rocks showing significant degree of hydrothermal alteration (i.e. complete destruction of magmatic textures and complete mineral replacement) were excluded.

2. Analytical Techniques

This study draws on 13 of the least-altered samples, including 9 volcanic and 4 intrusive rocks, from the Forest Reef Volcanics, collected and previously characterised by Squire (2001) and Squire and Crawford (2007; see Fig. 1)

Samples were collected from drill core and surface exposures throughout the Cadia-Neville region and were hand picked to exclude oxidised or weathered rinds, veins or amygdales. Samples cover a range of MgO contents, between 9.7 and 1.8 wt.% MgO, and were selected to trace the magmatic evolution of the suite. The PGE and Re concentration of samples were determined using the Ni-S fire assay–isotope dilution ICP-MS method. The PGE content of two mineralised quartz-calcite-sulfide veins (MQV) were also analysed for comparison with the Forest Reef Volcanic rocks (supplementary information, Table A.1).

2.1 Whole rock PGE and Re determination

Samples were powdered in an agate swing mill to minimize PGE contamination during crushing (Takamasa and Nakai, 2009) and analysed in three separate batches, along with duplicates, a procedural blank and the *TDB-1* (CCRMP-CANMET diabase) standard, following the Ni-S fire-assay isotope dilution method described by Park et al. (2012a).

The Ni-S fire-assay isotope method has three advantages over the Carius tube method when applied to the measurement of PGE in felsic rocks: (i) it avoids problems associated with acid digestion of refractory phases, (ii) it facilitates the use of large sample sizes, which reduces sampling problems caused by the nugget effect, and (iii) it removes elements that interfere with the PGE, notably Y, Zr and Mo that interfere with Pd, and Hf, and rare-earth elements (REE) that interfere with Pt.

The Ni-S fire-assay isotope dilution method involved mixing approximately 5 g of sample powder with Ni, S and sodium borax in the ratio sample:Ni:S:Na–borax = 10:1:0.5:10. A PGE-enriched spike solution (^{99}Ru, ^{105}Pd, ^{185}Re, ^{191}Ir and ^{195}Pt) was added to each unknown, blank and the *TDB-1* standard for internal standardization. Prepared powders were placed in porcelain crucibles, contained in a second larger crucible, dried at 100 °C and then fused at 1100 °C for 30 min. Reducing conditions were induced during fusion by placing ~5 g of wheat flour in outer crucibles and supplying a steady flow of N_2 gas into the furnace. Fusion concentrates PGE in the powdered sample into extractable Ni-S beads. After quenching, the Ni-S beads were separated from their glasses, weighed to assess recovery, and then dissolved by fluxing with 6M HCl in a conical flask at ~150 °C. After 5 hours of boiling in HCl, to ensure complete Ni-S bead dissolution, samples were removed, allowed to cool and filtered through Millipore (0.45 μm cellulose membrane) filter paper to extract un-dissolved PGE micro-nuggets. Filter papers were then digested in aqua regia and the solutions evaporated to incipient dryness (~100 μL). Finally solutions were diluted with 2% HNO_3, fluxed for 2 hours and centrifuged, prior to measurement by inductively coupled plasma mass spectrometry (ICP-MS).

Solutions were measured for PGE, Re and trace element isotopes using an Agilent 7700x Quadrupole ICP-MS at the Research School of Earth Sciences (RSES), Australian National University (ANU). Solutions, commencing with procedural blanks, were measured in order of increasing expected PGE and Re concentrations. Standard solutions were measured prior to, during and following unknown analyses to monitor instrumental drift and molecular interferences. Acid blanks were analysed between each analysis to assess background levels and 'memory' effects. The isotopes measured, length of analyses and dwell times were set to minimize molecular interferences yet maximize counting statistics and analytical sensitivities to 2.5–3.0 x 10^4 cps/ng/g for determination at the pg/g-level.

Data reductions and corrections (i.e. background, molecular interferences and mass bias) were performed following the methods of Park et al. (2012a). Briefly, all standards, procedural blank and unknown analyses were background corrected by subtracting average count rates from acid

blank analyses. Molecular interferences were monitored by measuring standard Ni, Cu, Zn, Co, Hf, Mo, Zr, Ta and V solutions and corrected for by subtracting argide and oxide production rates. Mass bias factors were determined from isotopic ratios of certified standard PGE and Re solutions. Background, molecular interference and mass bias corrections for all PGE and Re are generally less than 10%.

Absolute PGE and Re concentrations were determined by isotope dilution. Mono-isotopic ^{103}Rh was determined relative to ^{106}Pd, assuming that recovery rates for Rh are similar to Pd.

All unknown and *TDB-1* standard analyses were blank corrected by subtracting procedural blank averages. The PGE and Re concentrations of procedural blanks are detailed in the supplementary material (Table A.2). Batch 2 blank (*Blank-2*) contained higher than expected Ir, Rh, Pt and Re concentrations (see supplementary material, Table A.2). Close agreement between duplicate analyses of unknowns and the *TDB-1* standard from batch 2 with that of other batches (batch 1 and 3), however, suggest that only the blank was contaminated during sample preparation and therefore *Blank-2* was excluded from blank corrections.

Method detection limits (MDL), defined as three standard deviations of the procedural blanks, are 0.7 pg/g for Ir, 3.7 pg/g for Ru, 1.3 pg/g for Rh, 13 pg/g for Pt, 11 pg/g for Pd and 2.0 pg/g for Re (see supplementary material, Table A.2). All PGE and Re analyses were above the MDL, except for Ru in three samples (147-709D, 147-757D and 147-743).

Analytical accuracy and precision were assessed from multiple analyses of the *TDB-1* standard (see supplementary material, Table A.3). The *TDB-1* PGE and Re concentrations fall slightly below values reported by Ishikawa et al. (2014), Yang et al. (2014) and Chu et al. (2015), which were all measured using the Carius tube method. For example, Ir, Ru and Re were on average ~20% less, whereas Rh and Pt were ~10% less and Pd ~5% less. Nonetheless the *TDB-1* analyses from this study are consistent with values reported by other studies including Peucker-Ehrenbrink et al. (2003), Meisel and Moser (2004a), Park et al. (2013a, b) and Marchesi et al. (2014). The multiple *TDB-1* analyses (n=5) showed absolute differences of <0.05 ng/g for Ir, Ru

and Rh, which are present at low concentrations (<0.5 ng/g), and differences of no more than 1.2 ng/g for Pt and Pd, which are present at high concentrations (>4 ng/g), confirming the precision of the Ni-S isotope dilution ICP-MS technique.

Uncertainties in PGE and Re data mainly arise from sampling error due to the presence of PGE micro-nuggets, blank subtractions and ICP-MS counting statistics. Analytical uncertainties, determined by error propagation of ICP-MS counting statistics and background-, interference- and mass-bias- corrections, are quoted to 2σ and are generally <5% of absolute PGE concentrations. Ten duplicate analyses of Forest Reef Volcanic samples showed variances for Ir, Ru, Re, which are well above analytical error and attributed to sampling error caused by the presence of micro-nuggets (Table 1). The variances of Pt and Pd concentrations are lower (-34 to +13% relative) than those of Ir, Rh and Ru concentrations (-55 to +605% relative).

2.2 Homogeneity of Forest Reef Volcanic samples

The presence of micro-nuggets can complicate sampling and the measurement of precious metal concentrations, such as the PGE, particularly when these elements are present at low concentrations in the bulk rock (pg/g-level; Meisel and Moser, 2004b). The presence of one or more micro-nuggets in a sample aliquot is enough to significantly affect their measured concentration. Platinum group element-rich micro-phases such as platinum group minerals (PGM) and immiscible sulfide blebs have been shown to cause a heterogeneous distribution (i.e. 'nugget effect') at the 5 g sampling scale (e.g. Park et al., 2013b, 2015). The presence of such phases can be inferred from differences between duplicate analyses that lie beyond analytical uncertainty.

The PGE concentrations of samples analysed in this study are affected by the presence of micro-nuggets resulting in a difference in duplicate analyses that is beyond analytical error. Pt-rich nuggets in magnetite affect the PGE concentrations of the high-Mg samples, whereas immiscible sulfide melts affect the low-Mg samples. Differences between duplicate analyses are greatest for the PGE present in the lowest concentrations (1-200 pg/g) such as Ir, Ru and Rh. The relative difference in Ir, Ru and Rh concentrations, between duplicate analyses, vary up to 605%.

Differences between duplicate analyses for Pt and Pd are less (up to 13% relative), despite the presence of Pt-rich nuggets, because of their higher overall concentrations in the bulk rock (300-9000 pg/g).

Given the problem of the nugget effect, the duplicate aliquot containing the lowest PGE concentrations should always be used when making inferences about the PGE content of the magma. It is assumed that this sample will contain the lowest number of nuggets. However, this sample may still contain one or more nuggets and therefore the lowest measured concentration will represent the maximum possible concentration for the magma.

2.3 Analyses of magnetite and sulfides for PGE and major and trace elements

The major and trace element concentrations in magnetite grains from 10 samples and primary (magmatic) and secondary (hydrothermal) sulfides from 6 samples (pyrrhotite, pyrite, chalcopyrite) were then determined by electron microprobe analysis (EPMA) using a Cameca SX-100 at the RSES, ANU. The elements and x-ray lines used for both measurements were: Al (Kα), Si (Kα), S (Kα), Fe (Kα), Co (Kα), Ni (Kα), Cr (Kα), Cu (Kα), Zn (Kα) and Ag (Kα). The operating conditions were: accelerating voltage 15 kV, beam current 20 nA, beam diameter 5 μm. Analytical accuracy and precision was measured from multiple standard analyses of *Fe-metal*, *Chromite*, *Andradite* and Cr_2O_3 standards. Accuracy for all major and minor elements was better than 5% and precision better than 1% relative standard deviation (RSD) for most elements.

The PGE and trace element content of magnetite, from 8 samples, and secondary sulfides, from 4 samples, were measured by laser ablation inductively coupled plasma mass spectrometry (LA-ICP-MS) at the RSES, ANU. Primary sulfides, which are present as 5-15 μm wide spheroidal inclusions, were too small for measurement by LA-ICP-MS. The analytical system consisted of a Lambda Physik Complex 110 Excimer laser (λ=193 nm) and HelEX ablation cell coupled to an Agilent 7700x quadrupole ICP-MS. Spot analyses were carried out at a 5 Hz laser pulse rate, 45 ± 2 mJ output energy, using a 81 or 47 μm spot diameter. Spot analyses consisted of 15 s of background (Ar-gas blank) measurement, followed by 30 s of sample analysis. The isotopes

measured were ^{24}Mg, ^{27}Al, ^{29}Si, ^{45}Sc, ^{49}Ti, ^{51}V, ^{53}Cr, ^{55}Mn, ^{57}Fe, ^{59}Co, ^{61}Ni, ^{65}Cu, ^{66}Zn, ^{101}Ru, ^{103}Rh, ^{105}Pd, ^{189}Os, ^{192}Os, ^{193}Ir and ^{195}Pt.

The isotopes measured, volume ablated, length of ablation and integration times were all set to minimize potential interferences and maximize counting statistics. The *NIST 610* glass was used as an external standard for most of the trace elements and the USGS *MASS-1* synthetic polymetal sulfide standard was used for the PGE and Au. Only Pt, Ir and Os from the PGE could be quantified in magnetite and sulfide given that only these values are reported for *MASS-1* by the USGS. The Fe content obtained by EPMA was used as an internal standard for both trace elements and PGE determination. Data reduction was carried out using *Iolite v 3.31*. Molecular interferences on ^{103}Rh and ^{105}Pd caused by ^{63}Cu–^{40}Ar and ^{65}Cu–^{40}Ar, respectively, were monitored by measuring a Cu-metal standard and corrected for by subtracting argide production rates in pyrite and chalcopyrite. Molecular interference corrections are generally ~40% for ^{103}Rh and ^{105}Pd in pyrite and ~50% for ^{103}Rh and ~100% for ^{105}Pd in chalcopyrite. The corrected count rates for Pd in chalcopyrite analyses are at background-level indicating either i) no detectable Pd in chalcopyrite, or ii) over-correction due to different ^{105}Pd/^{65}Cu yield between Cu-metal and sulfide, coupled with high Cu-concentrations in chalcopyrite. Micro-phases, identified as spikes in time-resolved data, were omitted from integrations. Small sulfide grains, notably chalcopyrite, were often limited in their ablation time because of down-hole boring. Care was taken to ensure only count rates from sulfide, and not groundmass, were integrated.

Multiple analyses of the *NIST 610*, *NIST 612* and USGS *MASS-1* standards were used to assess the analytical accuracy during magnetite analysis. Results are presented in supplementary information Table A.4. The measured PGE and trace element concentrations, including Pt and Ir, generally agree within 2σ of the values from Jochum et al. (2011) and GEOREM. Multiple analyses of USGS *MASS-3* standard were used to assess the analytical accuracy during sulfide analysis. Results are presented in supplementary information Table A.5. The measured PGE and trace element contents, including Pt and Ir, agree within 2σ of the values reported by Fonseca et al. (2007).

3. Results

3.1 Whole rock major and trace elements

The whole rock major and trace element data used in this study were measured by X-ray Fluorescence (XRF) and ICP-MS by Squire (2001) and Squire and Crawford (2007), and are detailed in supplementary information, Table A.6 and are plotted in Fig 2 (a-f) and in supplementary material, Fig A.1 (a-e). All major element data are reported on an anhydrous basis with iron oxide as 100% Fe_2O_3.

The analysed samples are shoshonitic, varying from trachy-basalts to trachytes and follow a calc-alkaline evolution trend (Squire, 2001). The compositions of the samples range between 50 to 60 wt.% SiO_2, 13 to 19 wt.% Al_2O_3, 9.7 to 1.8 wt.% MgO, 11.3 to 5.6 wt.% Fe_2O_3 and 0.9 to 0.4 wt.% TiO_2.

Silica, Al_2O_3, Na_2O and K_2O increase with decreasing MgO, whereas CaO, Ni and Cr decrease (Fig. 2 (a-f) and supplementary information, Fig. A.1). Copper data show significant scatter when plotted against MgO and have no identifiable trend (supplementary information, Fig. A.1d). The scatter observed in MgO, the alkalis, CaO and Cu is attributed to hydrothermal alteration as indicated by the partial replacement of primary silicates (olivine, clinopyroxene, orthopyroxene, plagioclase) by secondary chlorite, epidote, sericite, calcite and albite, and the addition of secondary (hydrothermal) sulfides. Iron-oxide, TiO_2 and V initially increase with decreasing MgO, from 9.7 to 8.7 wt.%, then decrease with decreasing MgO. The coupled behaviour of Fe_2O_3, TiO_2 and V indicate the onset of magnetite saturation somewhere between 8.7 and 5.9 wt.% MgO as defined by samples 147-760 and 147-789, respectively. Three basaltic samples (147-767, 147-754 and 147-789), which fall below the general Fe_2O_3, TiO_2 and V fractionation trend, contain lower abundances of magnetite (<2% modal), relative to other basaltic samples (4-10% modal magnetite). This discrepancy makes it difficult to determine the timing of magnetite saturation, however it is best estimated at 8.7 wt.% MgO.

A primitive mantle normalized incompatible trace element diagram (Fig. 3) shows no Eu-anomaly and strong enrichment in the large ion lithophile elements (LILE), moderate enrichment in the light-REE (LREE) and slight enrichment in the heavy-REE (HREE) with respect to primitive mantle values (Sun and McDonough, 1989).

3.2 Whole rock PGE and Re concentrations

Whole rock PGE and Re concentrations for the Forest Reef Volcanics are listed in Table 1 and plotted against MgO in Fig. 4 (a-g). All PGE show tight co-variation with MgO (see Fig. 4 a-g) and a clear break is observed in the trends at 6.8 wt.% MgO. Above 6.8 wt.% MgO Pt and Pd are observed to increase, with decreasing MgO, whereas below 6.8 wt.% MgO both Pt and Pd decrease. Based on this contrast in PGE geochemistry, the Forest Reef Volcanics have been subdivided into the high-Mg (>6.8 wt.% MgO) and low-Mg samples (≤6.8 wt.% MgO).

The high-Mg samples contain between 4.2–9.3 ng/g Pd, 1.9–6.9 ng/g Pt and 0.01–0.25 ng/g Re. Rhenium abundances do not correlate well with MgO, but in general increase with decreasing MgO. The high-Mg samples contain lower concentrations of the remaining PGE, with 0.01–0.15 ng/g Ir, <0.003–0.28 ng/g Ru and 0.11– 0.27 ng/g Rh. The abundances of Ir and Ru decrease, whereas that of Rh remains constant with decreasing MgO, from 9.7 to 6.8 wt.%.

The low-Mg samples contain lower abundances of PGE than the high-Mg samples, with 1.3–6.5 ng/g Pd, 0.3–6.2 ng/g Pt, 0.001–0.016 ng/g Ir, 0.002–0.012 ng/g Ru, 0.006–0.14 ng/g Rh and 0.04–1.39 ng/g Re. Rhodium, like Pt and Pd, decreases with decreasing MgO, between 6.8 and 1.8 wt.%, in contrast to the high-Mg samples. Their behavior is similar to that of Ir and Ru, whose abundances continue to decrease, however at lower rates than during fractionation of the high-Mg samples. In contrast to the PGE, Re concentrations are an order of magnitude higher in the low-Mg than in the high-Mg samples.

Primitive Mantle (PM) normalized PGE and Re patterns for the Forest Reef Volcanics are shown in Fig. 5. The less evolved, high-Mg samples have PGE abundances comparable to Grenada Arc

Picrites. In contrast, the low-Mg samples are depleted in all PGE, but enriched in Re, relative to the high-Mg samples. Both high- and low-Mg samples have negative Ru anomalies.

Platinum-group element concentrations were measured in two mineralised quartz-calcite-sulfide veins (MQV). They vary between 4.8–19.8 ng/g Pd, 0.5 to 0.8 ng/g Pt, 0.002 to 0.005 ng/g Ir, 0.02 to 0.08 ng/g Ru, 0.02 to 0.05 ng/g Rh and 20 to 97 ng/g Re (Table 1). The mineralised quartz veins are enriched in Ru and Pd relative to the Forest Reef Volcanics (MQV/FRV= ~5.8 and ~2.7, respectively) and depleted in Rh, Ir and Pt (MQV/FRV = <0.5).

3.3 Magnetite and sulfide major and trace element geochemistry

Magnetite is observed in most samples and usually occurs as individual euhedral grains typically 80 to 100 μm in diameter and, more rarely, as smaller sized aggregates up to 100 μm in size. The proportion of magnetite varies from 10% modal in the high-Mg samples, to 4% modal in low-Mg samples.

Magmatic sulfide inclusions are observed only in the low-Mg samples (≤6.8 wt.% MgO) as 5–15 μm spheroidal inclusions of dominantly pyrite, pyrrhotite and rarely chalcopyrite in clinopyroxene, plagioclase and magnetite phenocrysts (Fig. 6 a-i). Sample 147-754 (6.8 wt.% MgO) is the most mafic sample in which spheroidal sulfide inclusions are found. This suggests sulfide saturation occurred around 6.8 wt.% MgO, which as shown later, is in agreement with the PGE geochemistry.

Secondary (hydrothermal) sulfides are dominated by pyrite with lesser chalcopyrite. Secondary sulfides are only observed in 5 out of the 13 samples and occur in trace (<1% modal) amounts. Pyrite grains are found as disseminated, euhedral (cubic) grains up to 50 μm in size. Chalcopyrite occurs as disseminated anhedral grains typically <20 μm, but with few up to 50 μm, in size.

The major element composition of magnetite is presented in supplementary material Table A.7, the data for primary (magmatic) sulfides in Table A.8 and secondary (hydrothermal) sulfides in Table A.9. Magnetite and both primary and secondary pyrite, pyrrhotite and chalcopyrite

compositions are typical of arc-related Fe-Ti oxides and sulfides (e.g. Ikehata et al., 2010; Velasco et al., 2016). The trace element and PGE content of magnetite is presented in supplementary information Table A.10, and that of secondary sulfides in Table A.11.

The concentration of PGE in magnetite was found to be at or slightly above detection limit values (supplementary information, Table A.10). Count rates of Rh, Ru, Ir and Pd are continuous in magnetite and are at or slightly above background levels (<10^1 CPS), whereas count rates of Pt occur as 'spikes' (10^2 to 10^3 CPS) in time-resolved data (supplementary information, Fig. A.2). Only Ir, Os and Pt concentrations could be quantified using the *MASS-1* external standard. Magnetite from two high-Mg samples contained Ir and Os concentrations of 8-9 ng/g and 0.2-0.7 ng/g, respectively, whereas these elements in the remaining samples fell below the detection limit of <4 ng/g and <0.2 ng/g, respectively. Given that Pt count rates are 'spiked', the concentration of Pt in magnetite could not be quantified. However, if the Pt-spikes were to be removed the Pt concentrations would fall below detection.

Only secondary (hydrothermal) sulfide grains were large enough for their trace elements to be measured by LA-ICP-MS. Platinum-group element concentrations in secondary sulfides (pyrite, chalcopyrite) were found to be at or below detection limit values (supplementary information, Table A.11). Count rates of Rh, Pd and Ru are continuous (10^0 to 10^3 CPS) in both pyrite and chalcopyrite, whereas count rates of Pt occur as 'spikes' in time-resolved data and Ir count rates fall slightly above or at background level (supplementary information, Fig A.3). Only Pt, Ir and Os could be quantified using the *MASS-1* external standard. Iridium and Os concentrations fell below their detection limits in all sulfide analyses (<2 ng/g and <0.2 ng/g, respectively). Because Pt count rates occur as 'spikes' in time-resolved data, the concentration of Pt in secondary sulfides was not quantified.

4. Discussion

4.1 Whole rock major and trace elements

The coherent trends formed by the major and trace elements suggest that the analysed samples, despite being classified into different units, experienced similar fractionation pathways and were sourced from a single magma chamber or similar parent magma chambers at depth.

The trace element signature of the Forest Reef Volcanics is characteristic of arc magmas and comparable to the continental arc signature of Rudnick and Fountain (1995; Fig. 3). A lack of Eu anomaly suggests that the parent magma did not fractionate plagioclase at depth. An alternative explanation for the lack of negative Eu anomaly is that the effect of plagioclase crystallisation was balanced by amphibole fractionation, which produces a positive Eu anomaly (Setiabudi, 2001), or by apatite or titanite fractionation (Fourcade and Allegre, 1981). Another factor that may be relevant is the fO_2 of the melt, which could have been high enough for Eu^{3+}, which has similar incompatibility to the other REE (Blevin, 2002), to be the dominant Eu species in the melt.

4.2 Identifying the timing of sulfide and volatile saturation

The aim of this study was to test the hypothesis that the timing of sulfide saturation, relative to volatile saturation, controls the Au-Cu fertility of an evolving felsic system. Before discussing the geochemistry of the PGE it is therefore necessary to identify the timing of these two critical events.

4.2.1 Timing and likely cause of sulfide saturation

Platinum and Pd abundances, in samples with MgO above 6.8 wt.%, increase with decreasing MgO, however decrease once the MgO falls below 6.8 wt.% (Fig. 4a-g). This change is attributed to the magma reaching sulfide saturation at 6.8 wt.% MgO. The precipitation of PGE-alloys or sulfide minerals are discounted for the following reasons: (i) Pd is not compatible in an alloy phase, (ii) sulfide inclusions are observed in liquidus minerals in low-Mg samples but not in the high-Mg samples, and (iii) the spherical shape of these sulfide inclusions indicates that the sulfide phase was in a molten-state at the time of entrapment.

The solubility of sulfur in a silicate melt, commonly described as the sulfur content at sulfide saturation (SCSS), is a function of temperature (T), pressure (P), melt composition (especially the

H_2O, Cu and Fe content of the melt), oxygen fugacity (fO_2) and sulfur fugacity (fS_2)(O'Neill and Mavrogenes, 2002; Liu et al., 2007). Sulfate is an order of magnitude more soluble than sulfide in a silicate melt (Jugo et al., 2005), hence the nature of the sulfur species, which is a function of the fO_2 of the melt, is also important. Sulfide is dominant in melts where $fO_2 \leq$ FMQ, whereas sulfate predominates if $fO_2 \geq$ FMQ+2 (Yang, 2012). The fO_2 of arc magmas, expressed as Δ FMQ, is +0.5 to +1.7 (Parkinson and Arculus, 1999). As a consequence sulfur will be present, at least in part, as sulfate with the estimated proportion of sulfate in arc magmas ranging from ca.20% of the total sulfur at fO_2 Δ FMQ = +0.5, to ca.80% at fO_2 Δ FMQ = +1.7 (Yang, 2012; references therein). The Forest Reef magma has been previously described as 'strongly oxidised' by Blevin (2002) but its fO_2 has not been quantified.

Although other factors may have contributed to sulfide saturation in the Forest Reef magma, a decrease in fO_2 associated with magnetite saturation appears to be the principal trigger. Magnetite saturation, as identified by the coincident depletion in Fe_2O_3, TiO_2 and V, starts at 8.7 wt.% MgO and is followed shortly after by sulfide saturation at 6.8 wt.% MgO, suggesting a genetic link between these processes. Magnetite precipitation lowers the Fe^{3+}/Fe^{2+} ratio of the silicate melt and therefore its fO_2, driving the reduction of sulfate to sulfide and triggering sulfide saturation (Jenner et al., 2010).

4.2.2 Timing of volatile saturation

Before it is emplaced into the upper crust, the magma that gives rise to a porphyry intrusion consists of a mixture of volatile-rich melt and crystals (e.g. Shinohara and Hendequist, 1997). Upon ascent, the magma will decompress and exsolve a volatile phase. The removal of this fluid phase lowers the solidus temperature of the porphyry causing it to quench. The fine-grained groundmass in a porphyritic sample therefore represents the composition of the magma at the time of volatile-saturation. The MgO content of the magma at the time of volatile saturation can therefore be estimated from the MgO content of the porphyry, after allowing for the MgO content of the phenocrysts.

Whole rock MgO values of the porphyry intrusions genetically associated with Au-Cu mineralisation in the Cadia district (Cadia Intrusive Complex; Holliday et al., 2002) range from 2.5 to 5.9 wt.% MgO (see supplementary information Table A.12). After deducting the MgO content of the Mg-rich phenocrysts (i.e. clinopyroxene, biotite, hornblende) and correcting for plagioclase, the resulting MgO content of the groundmass ranges from 1.1 and 2.9 wt.% MgO. This suggests that volatile saturation occurred at or slightly after the Forest Reef magma fractionated to 2.9 wt.% MgO.

4.3 Effects of hydrothermal overprinting on whole rock PGE

Iridium and Os concentrations in secondary sulfides (pyrite, chalcopyrite) are below the detection limit (supplementary information, Table A.11). Count rates of Rh, Pd and Ru are continuous, whereas count rates of Pt are 'spiked' indicating that Rh, Pd and Ru are held in the pyrite and chalcopyrite lattice whereas Pt is present as a Pt-rich micro-phase (supplementary information Fig. A.3). Despite not being able to quantify the concentrations of Rh or Pd, high count rates of Rh (10^1 to 10^2 CPS) indicate detectable concentrations in the sulfides whereas low count rates of Pd, slightly above or below detection (10^0 to 10^1 CPS) indicate negligible Pd concentrations in sulfides. Given (i) that only 5 out of the 13 of the analysed samples contained secondary (hydrothermal) sulfides, (ii) that where secondary sulfides are present their abundance is low (<1% modal), and (iii) that only a few secondary sulfide analyses contain PGE at or below detection, it is likely that the bulk of the PGE in these samples is magmatic and that little has been introduced during hydrothermal alteration. Rhodium is the most likely PGE to be affected by hydrothermal alteration since its count rates in pyrite and chalcopyrite are high (10^1 to 10^2 CPS) compared with the other PGE (10^0 to 10^1 CPS). However, the tight co-variation of the PGE with MgO confirms the hypothesis, that the PGE have been little affected by hydrothermal alteration. This is in sharp contrast to Cu, which shows considerable scatter when plotted against MgO (supplementary information, Fig. A.1d). Conversely, the removal of PGE during hydrothermal alteration is unlikely given the findings of Barnes and Liu (2012) who found that Pt and Pd are relatively immobile, irrespective of the nature and degree of alteration, especially in sulfide-poor, silicate rocks.

4.4 PGE variations in the high-Mg samples (>6.8 wt.% MgO)

Platinum, Pd and Re exhibit incompatible behaviour in the high-Mg rocks, whereas Ir, Ru, and to a lesser extent Rh, behave compatibly as MgO decreases from 9.7 and 6.8 wt.% (Fig 4 a-g). The enrichment in Pt and Pd requires the exclusion of these elements from early crystallising silicate and oxide phases, notably olivine, pyroxene and plagioclase. The strongly incompatible behavior of Pt and Pd during this period suggests that the magma did not experience early sulfide saturation.

The slope of Primitive Mantle (PM) normalized PGE patterns for the Cadia samples (Fig. 5) shows that the mantle source from which the primitive melt was derived was enriched in the PPGEs (Platinum-group PGE: Pt, Pd, Rh) and Re, relative to the IPGE. The negative Ru anomaly in the high-Mg samples can be attributed to early crystallisation of chromite at depth (Arguin et al., 2016).

The concomitant depletion of Ir and Ru in the high-Mg samples could be attributed to either: (i) saturation of a PGM phase directly from the silicate melt (e.g. Brenan and Andrews, 2001), (ii) partitioning of Ir and Ru into a spinel phase such as magnetite or chromite (e.g. Park et al., 2012b, 2016), or (iii) spinel-induced saturation of a Ir- and Ru-rich PGM micro-phase at the boundary of the growing crystal (e.g. Arguin et al., 2016).

Erlichmanite (OsS_2), laurite (RuS_2) and an IPGE-alloy (Brenan and Andrews, 2001) are significant hosts of the IPGE in mafic and ultra-mafic systems and the precipitation of one or more of these phases could account for the depletion of Ir and Ru in the high-Mg samples. The likelihood of erlichmanite cannot be evaluated due to a lack of Os data. Laurite can be discounted because the partitioning of Ir and Ru into laurite is Ru >> Rh ~ Ir (Brenan and Andrews, 2001), which contrasts with that observed in the high-Mg samples (Bulk D = Ir ~ Ru >> Rh).

Saturation of an IPGE-alloy depends on the solubility of Ir and Ru in a silicate melt, which decreases with decreasing fO_2, temperature and increasing Fe-content (Borisov and Palme, 2000). On the basis of the Borisov and Palme (2000) experiments, the solubility of Ir and Ru in a

felsic-intermediate oxidized magma (fO_2 = FMQ+1 to +2 and T = 700-900 °C) is approximately 1 µg/g Ir and 0.1 µg/g Ru (see supplementary material, Fig. A.4,). These solubilities are four to five orders of magnitude greater than the amount of Ir and Ru found in the highest-Mg samples (~0.04 ng/g), precluding the possibility of IPGE-alloy saturation and making precipitation of a PGM phase unlikely.

Iridium and Ru have been shown to partition into spinel phases, namely magnetite and chromite (e.g. Park et al., 2012b, 2016; Pagé and Barnes, 2016). Only magnetite is found in the samples used in this study. Magnetite is an inverse spinel phase and is expected to take Ir, Os, Ru and Rh into its structure (Park et al., 2017). Its precipitation is the most likely explanation for the observed depletion of Ir and Ru with decreasing MgO in the high-Mg samples (Fig. 4 b,d). The Ir and Os concentrations in magnetite, measured by LA-ICP-MS and reported in supplementary information Table A.10, support this hypothesis. The concentration of Ir and Os in magnetite from two of the high-Mg samples is 8-9 ng/g and 0.2-0.7 ng/g, respectively. The abundance of magnetite in these two samples, based on their Fe-content, and after allowing for the Fe-content of the co-existing silicate phases, is about 10 wt.%. As a consequence the bulk partition coefficient for Ir into magnetite in the high-Mg samples is probably above 1. Iridium and Os were not detected in magnetite in the low-Mg samples because, by this stage, crystal fractionation had decreased the concentration of Ir, and most likely Os, to a low-level.

Rhodium and Ru concentrations could not be quantified because there are no reported data for these elements in the external standard *MASS-1.* The compilation by Park et al. (2017) suggests that Ru has a higher partition coefficient into the inverse spinel structure than Rh, which would explain why Ru decreases with decreasing MgO, whereas Rh remains constant (Fig. 4 d,e.). In summary magnetite crystallisation provides the best explanation for the depletion of Ir, Ru and Rh with decreasing MgO in the high-Mg samples.

The count rates for Ir, Os, Ru and Rh during spot ablation of magnetite were constant, which suggests that Ir, Os, Ru and Rh are held in the magnetite lattice rather than in micro-phase inclusions such as an Ir-Ru-rich PGM (e.g. Arguin et al., 2016; Fig. A.2). In contrast, the count rates

for Pt have spikes suggesting the presence of Pt-rich micro-phase inclusions in magnetite. This phase may have precipitated in a localised reduction front, caused by magnetite crystallisation, similar to one that forms during chromite crystallisation (e.g. Arguin et al., 2016). The solubility of Pt is highly sensitive to fO_2 and can range from 130 ng/g to 0.8 ng/g at fO_2 between FMQ+2 to FMQ-2, respectively (Borisov and Palme, 2000). The Pt content of the silicate melt, at the time of magnetite saturation, was between 1.9 and 6.5 ng/g. Pt-alloy saturation therefore requires the localized oxygen fugacity in the magnetite crystallisation induced reduction front, to have fallen to below FMQ.

The ~2.9 and ~2.2 fold increase, of Pt and Pd respectively, between 9.7 to 6.8 wt.% MgO, is higher than expected from fractional crystallisation. The observed enrichments require 70% and 50% crystal fractionation, respectively, if both elements are perfectly incompatible. This is unlikely given the small decline in MgO (~2.9 wt.%) in the high-Mg samples. Because fractional crystallisation cannot account for the rate of Pt and Pd increase, other processes, namely assimilation and replenishment, must be considered. Crustal material typically contains <1 ng/g Pt and Pd (Park et al., 2012a; and references therein) so crustal contamination would decrease the PGE content of the magma and can therefore be ruled out.

Magma replenishment can prolong magmatic activity, facilitate eruption and modify magma geochemistry (Huppert and Sparks, 1981). It is common to most volcanic terranes including arc-environments (Anderson, 1976). Modelling (supplementary information, Fig. A.5) demonstrates that when lower fractions of replenishing magma are added to a system, the replenishing magma must contain higher Pt and Pd concentrations to explain the observed increase. For example, 10% and 20% replenishment requires the replenishing magma to have 65 and 11 ng/g Pt and 94 and 21 ng/g Pd, respectively. In contrast, 30 and 40% replenishment require only 18 and 3 ng/g Pt and 25 and 6 ng/g Pd, respectively. The highest Pd concentrations observed in primitive boninites and arc tholeiites is 38 ng/g (Hamlyn et al., 1985) rendering significant replenishment (>30%), by a magma only slightly more PGE enriched than the primary magma, the most likely scenario in the case of the Forest Reef Volcanics.

In the discussion that follows, the Rayleigh fractionation equation is used to model the low-Mg rocks, despite evidence of open-system behavior during the evolution of the high-Mg suite. Although there is no unambiguous evidence of open system behavior, during evolution of the low-Mg suite, we cannot dismiss this possibility. As a consequence, the modelling is not definitive and but rather serves to constrain magma evolution in the Forest Reef system.

4.5 PGE variations in the low-Mg samples (≤6.8 wt.% MgO)

4.5.1 Extent of fractional crystallisation in the low-Mg samples

Before modelling the evolution of the low-Mg samples, the amount of fractional crystallisation required to lower the MgO content of the melt from 6.8 to 1.8 wt.% must first be quantified. Two methods were used: first, the amount of fractional crystallisation required to raise the Zr content of the melt by the observed amount using the Rayleigh equation, and second, the amount required to lower its MgO content from 6.8 to 1.8 wt.% using Petrolog.

Zirconium was chosen because (i) it behaved as an incompatible element during magma evolution of the Forest Reef Volcanics (supplementary information Fig. A.1e), whereas other normally incompatible elements, such as P and La, did not, and (ii) because it shows the least amount of scatter when plotted against MgO relative to the other incompatible trace elements. Its tighter co-variation with MgO, relative to other incompatible elements, likely reflects its 'immobile' nature and its resistance to hydrothermal alteration. Despite this, some scatter in bulk rock Zr concentrations increases the uncertainty in the Zr concentration in the melt at a given MgO. A least-squares exponential curve was therefore fitted to the Zr data. The resulting curve (red trend, Figure A.1e), which has an R^2 value of 0.6, was used to estimate the evolution of the Zr concentrations in the Forest Reef Volcanics melt during Rayleigh crystal fractionation. The initial concentration of Zr (C_0) was set to that estimated by the least-squares model at 6.8 wt.% MgO to be 56 μg/g Zr. The bulk distribution coefficient (D_{Zr}) was calculated to be 0.27, assuming the proportion of plagioclase: clinopyroxene: amphibole: magnetite to be 60:29:10:1 and using partition coefficients from the literature (Fujimaki et al., 1984; Ewart and Griffin, 1994). These mineral proportions were calculated using the CIPW normative method of Johannsen (1931). The obtained mineral proportions were crosschecked by petrographic inspection assuming

closed system fractional crystallisation. The low-Mg rocks would have required ~54% crystal fractionation to raise the Zr content from 56 μg/g to 97 μg/g as the MgO decreases from 6.8 to 1.8 wt.% MgO.

The estimate of fractional crystallisation was crosschecked using the fractionation software model *Petrolog* (Danyushevsky and Plechov, 2011). The bulk starting composition was set to that of the most primitive low-Mg sample. *Petrolog* estimates ~52% fractionation is required to reduce the magma from 6.8 to 1.8 wt.% MgO, assuming fractionation of plagioclase, clinopyroxene, orthopyroxene and magnetite at a pressure of 4 kbar, 5 wt.% H_2O and an fO_2 of FMQ+1. This is in good agreement with ~54% fractionation estimated from the Zr modelling.

4.5.2 Effect of sulfide saturation on PGE variations in low-Mg samples

Fig. 7 compares the rate of depletion of Pd in the low-Mg samples with its rate of depletion in other felsic-intermediate systems that have been analysed for Pd. Note that the rate of depletion of Pd at Cadia is appreciable less than for any of the other S-saturated system shown in Fig. 7. If the rate of depletion of Pd, with its extreme partition coefficient into sulfide melts, is low, the rates of depletion of Au and Cu, with their lower partition coefficients, must be less and they may even become enriched by fractional crystallization. Either the Cadia S-saturated magma precipitated an unusually low fraction of immiscible sulfide melt or the sulfide melt failed to reach equilibrium with a sufficiently large volume of silicate melt. The latter occurs when R, the silicate-to-sulfide melt mass ratio, is much greater than D_{Pd}: the Pd sulfide-to-silicate melt partition coefficient. Both possibilities are considered.

4.5.3 Rayleigh Fractionation

The Rayleigh fractionation equation was used to model the post-sulfide saturation behavior of the PGE (Fig. 8a-e), assuming the volume of silicate melt the immiscible sulfide melt reached equilibrium was not a limiting factor (i.e $R >> D_{Pd}$). Only the analyses with the lowest PGE concentrations from duplicate analyses were used to define the modeled trend lines because these samples are interpreted to contain the lowest concentration of 'nuggets', therefore providing a more accurate estimate of PGE concentrations in the Forest Reef magma. Model 1

(blue) assumes fractionation of a typical silicate and oxide assemblage (plag:cpx:amp:mag = 60:29:10:1), with the starting concentrations set to that of the most primitive low-Mg sample (6.8 wt.% MgO), again using partition coefficients from the literature (supplementary material, Table A.13). Model 2 (red) accounts for the fractionation of an immiscible sulfide. If $D_{Pd}^{sul\text{-}sil}$ is taken to be 10^5 (Mungall and Brenan, 2014) the fraction of sulfide melt required to obtain the best fit to the data is 0.003 wt.%. At this fraction of sulfide melt, the partition coefficients required to model the depletion of the remaining PGE vary between 10^4 to 10^5, which lie within the low end of the range proposed by Mungall and Brenan (2014; i.e. $D_{PGE}^{sul} \sim 10^5$ to 10^6). However, the fraction of sulfide required is one- to two-orders of magnitude less than normally found in felsic systems (0.15 to 0.3 wt.%; Hao et al., 2017).

4.5.4 Finite reservoir fractionation

An alternative approach is to use the experimentally derived equation of Liu et al. (2007) to calculate the sulfur content of the melt at sulfur saturation (SCSS) and use this value to calculate the apparent partition coefficient required to produce the observed Pd vs. MgO trend (Fig. 4c). The Liu et al. (2007) equation is:

$$\ln(S\ ng/g)_{SCSS} = 11.35251 - \frac{4454.6}{T} - 0.03190\ \frac{P}{T} + 7.1006 \ln(MFM) - 1.98063\left[(MFM)\left(X_{H_2O^{melt}}\right)\right] + 0.21867 \ln\left(X_{H_2O^{melt}}\right) + 0.36192 \ln X_{FeO^{melt}} \quad (1)$$

where T is temperature in Kelvin, P is pressure in bars and MFM is a parameter describing the melt composition in terms of cation mole fractions:

$$MFM = \frac{Na+K+2(Ca+Mg+Fe^{2+})}{Si \times (Al+Fe^{3+})} \quad (2)$$

The Liu et al. (2007) model was used in preference to the Li and Ripley (2005), and Holzheid and Grove (2002) models because it takes into account the influence of pressure, temperature, water concentration and fO_2 on the SCSS in natural basaltic to rhyolitic melts by using both experimental data from their study and data from the literature. The composition of the melt used was that of the bulk rock composition of the most primitive low-Mg sample (147-754 at 6.8 wt.% MgO; see supplementary material Table A.6). The temperature of the Forest Reef Volcanics at 6.8 wt.% MgO is assumed to be ~800 °C, the H_2O content ~5 wt.% and the pressure ~4 kbar.

Under these conditions, the Liu et al. (2007) equation estimates that the SCSS of the Forest Reef Volcanics to be 110 µg/g S. The stoichiometry of the sulfide melt in the Forest Reef Volcanics, as determined by EPMA, is $Fe_{0.34}S_{0.61}Cu_{0.05}$. Assuming this stoichiometry, the calculated S content of the melt converts to 0.023 wt.% sulfide melt. This is an order of magnitude greater than that calculated from the rate of Pd depletion (0.003 wt.% sulfide), assuming a $D_{Pd}^{sul} \sim 10^5$.

The caveat of using the Liu et al. (2007) equation is that the pressure and temperature range of their experiments (1150 to 1450 °C and 500 MPa to 1 GPa) were higher than those assumed for the Forest Reef magma (~800 °C and 400 MPa). Nevertheless the estimated SCSS from the equation is intermediate between those calculated from the Li and Ripley (2005), and Holzheid and Grove (2002) models and within the range expected for granitic magmas (Yang, 2012). The cause of the low SCSS of the Forest Reef Volcanics magma is uncertain but it maybe that its fO_2 is closer to FMQ than assumed by Blevin (2002).

If the amount of sulfide melt to have precipitated following sulfide saturation was 0.023 wt.%, the partition coefficient required to account for the depletion of Pd, with decreasing MgO, is 1.4 x 10^4. This partition coefficient is at least an order of magnitude lower than those measured by Mungall and Brenan (2014; i.e. $D_{PGE}^{sul} \sim 10^5$ to 10^6), which suggests that the mass of silicate melt the sulfide melt reached equilibrium with was a limiting factor. It is therefore an *apparent* partition coefficient (*D'*) controlled by *R* (Campbell and Naldrett, 1979).

In a dynamic, open-system, the *R* is defined as the mass ratio of silicate melt a sulfide droplet of given mass can equilibrate with prior to being removed from the silicate melt (Mungall, 2002). The degree to which a droplet of sulfide melt attains chemical equilibrium with a body of silicate melt is dependent on a number of kinetic factors, including: the diffusion rate of metals through a silicate melt, the radius of the droplet, the velocity with which the droplet is advected through the melt and the duration of the co-existing phases (Mungall, 2002). It is not practical to calculate the effective *R* from first principles because diffusion rates of the PGE are poorly known and the mass of silicate melt a sulfide droplet reaches equilibrium with before it settles, varies between droplets, especially if the velocity of the convecting magma exceeds the settling rate of the

droplet. In this case the sulfide droplet may be carried through more than one cycle of convection before it settles (Martin and Nokes, 1989).

Fortunately the average R in an open-system can be calculated from D'. Campbell and Naldrett (1979) proposed the following equation for quantifying the relationship between R and D:

$$C_i^{sul} = C_i^{sil} D_i (R + 1)/(R + D_i) \quad (3)$$

where C_i^{sul} is the concentration of element i in the sulfide liquid, C_i^{sil} is its concentration in the silicate melt and D_i is its partition coefficient between the sulfide and silicate melt. From eq. (3) it follows that:

$$D_i' = C_i^{sul} / C_i^{sil} = D_i (R + 1)/(R + D_i) \quad (4)$$

where D_i' is the apparent partition coefficient of element i between the sulfide and silicate melt. It can be shown from eq. (4) that if $R > 10xD_i$, then $D_i' \sim D_i$, whereas if $D_i > 10xR$, then $D_i' \sim R$. Between these two extremes both D_i and R affect D_i'. Because D_{Pd}' (1.4×10^4) is much less that D_{Pd} (10^5 to 10^6), $R \sim D_{Pd}' = 1.4 \times 10^4$. Taking the value of R to be 1.4×10^4 and assuming $D_{Cu}^{sul\text{-}sil} \sim 1500$ and $D_{Au}^{sul\text{-}sil} \sim 8000$ (Mungall and Brenan, 2014) the calculated values for $D'_{Cu}{}^{sul}$ and $D'_{Au}{}^{sul}$, from eq. (4) are ca.1400 and ca. 5200, respectively.

4.5.5 Implications of sulfide saturation for Cu and Au fractionation

Fig. 9 shows the effect of Rayleigh fractionation on the concentration of Pd, Au and Cu in the evolving Forest Reef Volcanics assuming (a) equilibrium fractional crystallization ($R >> D_{Pd}$), and (b) finite volume fractional crystallization ($R \sim D_{Pd}' = 1.4 \times 10^4$). In both cases sulfide saturation is assumed to start at F = 0.34 and the rate of sulfide precipitation to increase gradually over 10% fractionation, as seen in the Skaergaard Intrusion (Keays and Tegner, 2016), to the maximum amount of 0.003 wt. % (model a) or 0.023 wt.% (model b) sulfide melt. The partition coefficients used for model (a) were $D_{PGE}^{sul\text{-}sil} \sim 10^5$, $D_{Au}^{sul\text{-}sil} \sim 8000$ and $D_{Cu}^{sul\text{-}sil} \sim 1500$ (Mungall and Brenan, 2014), whereas those for model (b) were $D'_{PGE}{}^{sul\text{-}sil} \sim 10^4$, $D'_{Au}{}^{sul\text{-}sil} \sim 5200$ and $D'_{Cu}{}^{sul\text{-}sil} \sim 1400$. The net enrichment in Au and Cu between the initial concentrations and the concentration at volatile saturation (F= 0.65) are x3.8 and x4.8 for Au and Cu, respectively, for model (a) and x1.2 and x3.5 for model (b; Fig. 10). The equilibrium model (a) concentrates both Au and Cu prior to volatile saturation, which is consistent with Cadia being a Au-Cu deposit but the low amount of sulfide

required to have precipitated by this model makes it questionable. Model (b) has a more realistic amount of sulfide precipitation. Copper is enriched by fractional crystallization but Au is not, which is unexpected if the parent magma is to form Au-Cu mineralisation (Fig. 10). Either the parent magma had an unusually high Au/Cu ratio or the high Au/Cu of the Cadia ore is the product of hydrothermal rather than magmatic processes.

A third model (not shown) explored the implications of a higher rate of sulfide precipitation (0.15 wt.%). The Au in this model drops to x0.15 of the initial Au concentration, at the time of volatile saturation, and Cu to x0.67, making the formation of an Au-Cu deposit highly unlikely. This is because the higher the fraction of immiscible sulfide melt assumed in the calculation, the lower R must be to model the observed depletion rate for Pd. The lower the value of R the higher the depletion rate of Au and Cu (compare Fig. 9a and b). It is difficult to escape the conclusion that the amount of immiscible sulfide melt to have precipitated in the Forest Reef magma was less than that of the other sulfide saturated felsic-intermediate systems.

4.5.6 PGE variations in Cadia ore veins: Implications for PGE mobility in magmatic-hydrothermal fluids

The solubility of PGE in saline solutions is several orders of magnitude lower than that of Au, Cu, Ni and Fe (Simon and Pettke, 2009; Tagirov et al., 2013; Park et al., 2016). The solubility of Pd in brine is ~1 ng/g (Tagirov et al., 2013), whereas that of Au is 0.3-0.8 μg/g and Cu is 0.3-0.8 wt.% (Ulrich et al., 1999). Despite this, several porphyry Au-Cu deposits are known to host significant amounts of PGE although not at economic concentrations (e.g., Eliopoulos and Economou-Eliopoulos, 1991; Tarkian and Koopmann, 1995; Tarkian and Stribrny, 1999). The partitioning of the individual PGE into magmatic volatile phases is poorly understood, but porphyry deposits are enriched in the PPGE but not the IPGE (e.g. Ir <1 ng/g; Pd/Ir~10^2 to 10^4; Park et al., 2016 and references therein), and are more enriched in Pd than Pt, with Pd/Pt ranging from 7 to 60 (Park et al., 2016). High Pd/Pt ratios have been interpreted to indicate that Pd is more soluble than Pt in magmatic-hydrothermal fluids (Augé et al., 2005).

A recent study by Park et al. (2016), who measured the PGE concentrations in Niuatahi-Motutahi ocean-floor sublimates, suggests that Pt is more soluble than Pd in magmatic-hydrothermal fluids and that the high Pd/Pt of ore-forming fluids is inherited from the parent magma, which has a high Pd/Pt as a result of early Pt-alloy precipitation.

The results of this study are inconsistent with the findings of Park et al. (2016). Instead they support the conventional interpretation that Pd is more soluble than Pt. Two mineralised quartz-calcite-sulfide veins were analysed, in duplicate, from the Cadia region. The Pd/Pt of these veins range from 10 to 31, which is typical of porphyry deposits. In contrast, the Pd/Pt of the most evolved Forest Reef Volcanic samples, which contain <5 wt.% MgO, range between 4 and 8. The two- to three-fold higher Pd/Pt of the ore-veins, compared with the Forest Reef Volcanics, suggests that Pd is more soluble than Pt in magmatic-hydrothermal fluids and that the high Pd/Pt is not inherited from the magma. A comparison of the PGE concentrations in the mineralised quartz vein and magmatic rocks analysed in this study, shows the solubility of the PGE in the Cadia magmatic-hydrothermal fluids is Ru > Pd > Rh > Ir > Pt. Irrespective of their different solubilities, the PGE are not as mobile as Au and Cu and must therefore become highly concentrated in a fractionating magma before they can make a significant contribution to the mineralisation in a porphyry system (Park et al., 2016).

5. Conclusions

A decrease in the PGE concentrations in the Forest Reef Volcanics, during magmatic differentiation, indicates that sulfide saturation occurred at around 6.8 wt.% MgO, about 4 wt.% MgO before volatile saturation. Although sulfide saturation occurred earlier in the Forest Reef Volcanics than in other ore-associated suites, the rate Pd depletion is appreciably less. Either the amount of sulfide melt to have precipitated was unusually low and/or the sulfide melt reached equilibrium with a limited volume of silicate melt so that the silicate-to-sulfide mass ratio is a significant factor. The evolution of Pd, Au and Cu, in the low-Mg samples can be modeled if the silicate melt precipitated 0.023 wt.% sulfide melt, provided the sulfide melt extracted these elements from a finite volume of silicate melt, ~1.4×10^4 times that of the sulfide melt. This fraction of sulfide melt is small compared to that found in other sulfide saturated felsic-

intermediate systems (e.g. Park et al., 2013a; Cocker et al., 2016; Hao et al., 2017) but it is large enough to produce a small reduction in the PGE content of the silicate melt with fractionation without reducing its Cu or Au content. This is because of the differences in the partition coefficients of these elements into the sulfide melt ($D_{PGE} > D_{Au} > D_{Cu}$; Mungall and Brenan, 2014). Despite sulfide saturation, Cu would have increased by x3.5 its initial concentration in the melt and Au by x1.2, following the ~65% fractionation required to reduce the MgO content of the melt from 9.7 to 2.9 wt.%. The bulk of Cu and Au in the silicate melt would have therefore been available to enter the magmatic-hydrothermal fluid at the time of volatile saturation. Nevertheless the observation that the mineralisation at Cadia has a high Au/Cu ratio suggests that either the Au/Cu ratio of the parent magma was unusually high or that hydrothermal processes played an important role in controlling the nature of the mineralization.

This study demonstrates that sulfide saturation does not necessarily adversely impact the fertility of a magma provided the fraction of sulfide to form is small so that the bulk partition coefficients for Cu and Au are less than 1, or that the fractionation interval between sulfide and volatile saturation is small. It also highlights the important role of fractional crystallisation in concentrating Cu and Au in the parent magma, until the point of volatile saturation.

Acknowledgements

This research was funded by a Newcrest Mining LTD Grant to Ian Campbell. The samples used in this study were collected by Richard J. Squire from the ARC Centre for Excellence in Ore Deposits (CODES), University of Tasmania (UTas), Hobart, Tasmania, Australia. We would like to thank Nathan Fox (CODES, UTas) for supplying mineralised samples and the staff at CODES, UTas for their help in acquiring samples. We also would like to thank Anthony Harris of Newcrest Mining LTD for supporting this project.

References

Anderson, A.T. 1976. Magma mixing: petrological process and volcanological tool. *Journal of Volcanology and Geothermal Research* **1**, 3–33.

Arguin, J. P., Pagé, P., Barnes, S. J., Yu, S. Y., and Song, X. Y. 2016. The effect of chromite crystallization on the distribution of osmium, iridium, ruthenium and rhodium in picritic magmas: an example from the Emeishan Large Igneous Province, Southwestern China. *Journal of Petrology* ***57*****,** 1019-1048.

Augé, T., Genna, A., Legendre, O., Ivanov, K.S., and Volchenko, Y.A. 2005. Primary Platinum Mineralization in the Nizhny Tagil and Kachkanar Ultramafic Complexes, Urals, Russia: A Genetic Model for PGE Concentration in Chromite-Rich Zones. *Economic Geology* **100**, 707–732.

Bai, W., Robinson, P.T., Fang, Q., Yang, J., Yan, B., Chang, Z., Hu, X.-F., Zhou, M.-F., and Malpas, J. 2000. The PGE and Base-Metal Alloys in the Podiform Chromitites of the Luobusa Ophiolite, Southern Tibet. *The Canadian Mineralogist* **38**, 585–598.]

Barnes, S. J., and Liu, W. 2012. Pt and Pd mobility in hydrothermal fluids: evidence from komatiites and from thermodynamic modelling. *Ore Geology Reviews* **44**, 49-58.

Barnes, S.J., and Maier, W. 1999. The fractionation of Ni, Cu and the noble metals in silicate and sulfide liquids. *Geological Association of Canada Short Course Notes* **13**, 69–106.

Blevin, P.L. 2002. The petrographic and compositional character of variably K-enriched magmatic suites associated with Ordovician porphyry Cu–Au mineralisation in the Lachlan Fold Belt, Australia. *Mineralium Deposita* **37**, 87–99.

Borisov, A., and Palme, H. 1997. Experimental determination of the solubility of platinum in silicate melts. *Geochimica et Cosmochimica Acta* **61**, 4349–4357.

Borisov, A., and Palme, H. 2000. Solubilities of noble metals in Fe-containing silicate melts as derived from experiments in Fe-free systems. *American Mineralogist* **85**, 1665–1673.

Brenan, J.M., and Andrews, D. 2001. High-temperature stability of laurite and Ru-Os-Ir alloy and their role in PGE fractionation of mafic magmas. *The Canadian Mineralogist* **39**, 341–360.

Brenan, J.M., McDonough, W., and Dalpe, C. 2003. Experimental constraints on the partitioning of rhenium and some platinum-group elements between olivine and silicate melt. *Earth and Planetary Science Letters* **212**, 135–150.

Brenan, J.M., McDonough, W.F., and Ash, R. 2005. An experimental study of the solubility and partitioning of iridium, osmium and gold between olivine and silicate melt. *Earth and Planetary Science Letters* **237**, 855–872.

Brenan, J.M., Finnigan, C.F., McDonough, W.F., and Homolova, V. 2012. Experimental constraints on the partitioning of Ru, Rh, Ir, Pt and Pd between chromite and silicate melt: the importance of ferric iron. *Chemical Geology* **302**, 16–32.

Campbell, I.H., Naldrett, A.J. 1979. The influence of silicate: sulfide ratios on the geochemistry of magmatic sulfides. *Economic Geology* **74**, 1503–1506.

Campbell, I.H., Naldrett, A.J., and Barnes, S.J. 1983. A Model for the origin of the platinum-rich sulfide horizons in the Bushveld and Stillwater Complexes. *Journal of Petrology* **24**, 133–165.

Capobianco, C., and Drake, M. 1994. Partitioning and solubility of PGEs in oxides and silicates. *Mineral. Magazine A* **58**, 144–145.

Capobianco, C.J., Hervig, R.L., and Drake, M.J. 1994. Experiments on crystal/liquid partitioning of Ru, Rh and Pd for magnetite and hematite solid solutions crystallized from silicate melt. *Chemical Geology* **113**, 23–43.

Carmichael, I.S.E. 1996. The iron-titanium oxides of salic volcanic rocks and their associated ferromagnesian silicates. *Contributions to Mineralogy and Petrology* **14**, 36–64.

Chazey, W.J., and Neal, C.R. 2005. Platinum-group element constraints on source composition and magma evolution of the Kerguelen Plateau using basalts from ODP Leg 183. *Geochimica et Cosmochimica Acta* **69**, 4685–4701.

Chu, Z., Yan, Y., Chen, Z., Guo, J., Yang, Y., Li, C., and Zhang, Y. 2015. A Comprehensive Method for Precise Determination of Re, Os, Ir, Ru, Pt, Pd Concentrations and Os Isotopic Compositions in Geological Samples. *Geostandards and Geoanalytical Research* **39**, 151–169.

Cocker, H.A., Valente, D.L., Park, J.W., Campbell, I.H. 2016. Using Platinum Group Elements to Identify Sulfide Saturation in a Porphyry Cu System: the El Abra Porphyry Cu Deposit, Northern Chile. *Journal of Petrology* **56**, 2491–2514.

Cooke, D.R., Wilson, A., House, M., Wolfe, R., Walshe, J., Lickfold, V., and Crawford, A. 2007. Alkalic porphyry Au – Cu and associated mineral deposits of the Ordovician to Early Silurian Macquarie Arc, New South Wales. *Australian Journal of Earth Sciences* **54**, 445–463.

Crawford, A.J. 2007. Geochemistry and age of magmatic rocks in the unexposed Narromine, Cowal and Fairholme Igneous Complexes in the Ordovician Macquarie Arc, New South Wales. *Australian Journal of Earth Sciences* **54**, 243–271.

Danyushevsky, L. V. and Plechov, P. 2011. Petrolog3: Integrated software for modeling crystallization processes. *Geochem. Geophys. Geosyst.* **12**, http://dx.doi.org/10.1029/2011GC003516.

Eliopoulos, D.G., and Economou-Eliopoulos, M. 1991. Platinum-group element and gold contents in the Skouries porphyry copper deposit, Chalkidiki Peninsula, northern Greece. *Economic Geology*, **86**, 740-749.

Ewart, A., and Griffin, W.L. 1994. Trace-element partitioning with application to magmatic processes application of proton-microprobe data to trace-element partitioning in volcanic rocks. *Chemical Geology* **117**, 251–284.

Fonseca, R. O., Mallmann, G., O'Neill, H. S. C., and Campbell, I. H. 2007. How chalcophile is rhenium? An experimental study of the solubility of Re in sulphide mattes. *Earth and Planetary Science Letters* **260**, 537-548.

Fourcade, S., and Allegre, C. J. 1981. Trace elements behavior in granite genesis: A case study The calc-alkaline plutonic association from the Querigut complex (Pyrénées, France). *Contributions to Mineralogy and Petrology* **76**, 177-195.

Fox, N., Cooke, D.R., Harris, A.C.H., Collet, D., and Eastwood, G. 2015. Porphyry Au-Cu mineralization controlled by reactivation of an arc-transverse volcano-sedimentary sub-basin. *Geology*, **43**, 811-814.

Fujimaki, H., Tatsumoto, M. and Aoki, K. 1984. Partition coefficients of Hf, Zr, and REE between phenocrysts and groundmasses. *Journal of Geophysical Research* ***89****, 662-672*

Glen, R.A., Walshe, J.L., Barron, L.M., and Watkins, J.J. 1998. Ordovician convergent-margin volcanism and tectonism in the Lachlan sector of east Gondwana. *Geology* **26**, 751–754.

Govindaraju, K. 1994. Compilation of working values and sample description for 383 geostandards. *Geostandards and Geoanalytical Research* **18**, 1–158.

Hamlyn, P.R., Keays, R.R., Cameron, W.E., Crawford, A.J., and Waldron, H.M. 1985. Precious metals in magnesian low-Ti lavas: Implications for metallogenesis and sulfur saturation in primary magmas. *Geochimica et Cosmochimica Acta* **49**, 1797–1811.

Hao, H., Campbell, I.H., Park, J.W., and Cocker, D.R. 2017. Platinum-group element geochemistry used to determine Cu and Au fertility in the Northparkes igneous suites, New South Wales, Australia. *Geochimica et Cosmochimica Acta* **216**, 372–392.

Harris, A.C., Percival, I.G., Cooke, D.R., Tosdal, R.M., Fox, N., Allen, C.M., Tedder, I., McMillan, C., Dunham, P., and Collett, D. 2014. Marine volcanosedimentary basins hosting porphyry Au-Cu deposits, Cadia Valley, New South Wales, Australia. *Economic Geology* **109**, 1117–1135.

Hill, E., Wood, B.J., and Blundy, J.D. 2000. The effect of Ca-Tschermaks component on trace element partitioning between clinopyroxene and silicate melt. *Lithos* **53**, 203–215.

Holliday, J.R., Wilson, A.J., Blevin, P.L., Tedder, I.J., Dunham, P.D., and Pfitzner, M. 2002. Porphyry gold–copper mineralisation in the Cadia district, eastern Lachlan Fold Belt, New South Wales, and its relationship to shoshonitic magmatism. *Mineralium Deposita* **37**, 100–116.

Holzheid, A., and Grove, T. 2002. Sulfur saturation limits in silicate melts and their implications for core formation scenarios for terrestrial planets. *American Mineralogist* **87**, 227.

Huppert, H.E., and Sparks, R.S.J. 1981. The fluid dynamics of a basaltic magma chamber replenished by influx of hot, dense ultrabasic magma. *Contributions to Mineralogy and Petrology* **75**, 279–289.

Ikehata, K., Yasuda, A., and Notsu, K. 2010. The geochemistry of volatile species in melt inclusions and sulfide minerals from Izu-Oshima volcano, Japan. *Mineralogy and Petrology* ***99***, 143-152.

Ishikawa, A., Senda, R., Suzuki, K., Dale, C.W., and Meisel, T. 2014. Re-evaluating digestion methods for highly siderophile element and 187Os isotope analysis: Evidence from geological reference materials. *Chemical Geology* **384**, 27–46.

Jenner, F.E., O'Neill, H.S.C., Arculus, R.J., and Mavrogenes, J.A. 2010. The Magnetite Crisis in the evolution of arc-related magmas and the initial concentration of Au, Ag and Cu. *Journal of Petrology* **51**, 2445–2464.

Jochum, K.P., Weis, U., Stoll, B., Kuzmin, D., Yang, Q., Raczek, I., Jacob, D.E., Stracke, A., Birbaum, K., Frick, D.A. and Günther, D. 2011. Determination of reference values for NIST SRM 610–617 glasses following ISO guidelines. *Geostandards and Geoanalytical Research* **35**, 397-429.

Johannsen, A. 1931. A Descriptive Petrography of the Igneous Rocks. Volume 1 (p. 88-92). University of Chicago Press, Chicago, 267 p.

Jugo, P.J., Luth, R.W., and Richards, J.P. 2005. An experimental study of the sulfur content in basaltic melts saturated with immiscible sulfide or sulfate liquids at 1300° C and 1.0 GPa. *Journal of Petrology* **46**, 783–798.

Jugo, P.J. 2009. Sulfur content at sulfide saturation in oxidized magmas. *Geology* **37**, 415–418.

Kamenetsky, V.S., Park, J.W., Mungall, J.E., Pushkarev, E.V., Ivanov, A.V., Kamenetsky, M.B. and Yaxley, G.M. 2015. Crystallization of platinum-group minerals from silicate melts: Evidence from Cr-spinel–hosted inclusions in volcanic rocks. *Geology* **43**, 903–906.

Keays, R.R. and Tegner, C. 2016. Magma chamber processes in the formation of the low-sulphide magmatic Au–PGE mineralization of the Platinova Reef in the Skaergaard Intrusion, East Greenland. *Journal of Petrology*, **56**, 2319-2340.

Kress, V.C., and Carmichael, I.S. 1991. The compressibility of silicate liquids containing Fe_2O_3 and the effect of composition, temperature, oxygen fugacity and pressure on their redox states. *Contributions to Mineralogy and Petrology* **108**, 82–92.

Large, R. R., Gemmell, J. B., Paulick, H., and Huston, D. L. 2001. The alteration box plot: A simple approach to understanding the relationship between alteration mineralogy and lithogeochemistry associated with volcanic-hosted massive sulfide deposits. *Economic geology* ***96***, 957-971.

Li, C., and Ripley, E.M. 2005. Empirical equations to predict the sulfur content of mafic magmas at sulfide saturation and applications to magmatic sulfide deposits. *Mineralium Deposita* **40**, 218–230.

Liu, Y., Samaha, N.T., and Baker, D.R. 2007. Sulfur concentration at sulfide saturation (SCSS) in magmatic silicate melts. *Geochimica et Cosmochimica Acta* **71**, 1783–1799.

Lowenstern, J.B. 2001. Carbon dioxide in magmas and implications for hydrothermal systems. *Mineralium Deposita* **36**, 490–502.

Mallman, G., and O'Neill, H.S.C. 2007. The effect of oxygen fugacity on the partitioning of Re between crystals and silicate melt during mantle melting. *Geochimica et Cosmochimica Acta* **71**, 2837–2857.

Marchesi, C., Dale, C.W., Garrido, C.J., Pearson, D.G., Bosch, D., Bodinier, J.L., Gervilla, F., and Hidas, K. 2014. Fractionation of highly siderophile elements in refertilized mantle: Implications for the Os isotope composition of basalts. *Earth and Planetary Science Letters* **400**, 33–44.
Martin, D., and Nokes, R. 1989. A fluid-dynamical study of crystal settling in convecting magmas. *Journal of Petrology* **30**, 1471-1500.

Meisel, T., Fellner, N., and Moser, J. 2003. A simple procedure for the determination of platinum group elements and rhenium (Ru, Rh, Pd, Re, Os, Ir and Pt) using ID-ICP-MS with an inexpensive on-line matrix separation in geological and environmental materials. *Journal of Analytical Atomic Spectrometry* **18**, 720.

Meisel, T., and Moser, J. 2004a. Platinum-Group Element and rhenium concentrations in low abundance reference materials. *Geostandards and Geoanalytical Research* **28**, 233–250.

Meisel, T., and Moser, J. 2004b. Reference materials for geochemical PGE analysis: new analytical data for Ru, Rh, Pd, Os, Ir, Pt and Re by isotope dilution ICP-MS in 11 geological reference materials. *Chemical Geology* **208**, 319–338.

Mukherjee, R., Mondal, S.K., Zhong, H., Bai, Z.J., Balaram, V., and Ravindra Kumar, G.R. 2014. Platinum-group element geochemistry of komatiite-derived 3.1 Ga ultramafic–mafic rocks and chromitites from the Nuggihalli greenstone belt, Western Dharwar craton, India. *Chemical Geology* **386**, 190–208.

Mungall, J.E. 2002. Kinetic controls on the partitioning of trace elements between silicate and sulfide liquids. *Journal of Petrology* **43**, 749–768.

Mungall, J.E., and Brenan, J.M. 2014. Partitioning of platinum-group elements and Au between sulfide liquid and basalt and the origins of mantle-crust fractionation of the chalcophile elements. *Geochimica et Cosmochimica Acta* **125**, 265–289.

Naldrett, A.J., and Duke, J.M. 1980. Platinum metals magmatic sulfide ores. *Science* **208**, 1417–1424.

Naldrett, A.J. 1999. World-class Ni-Cu-PGE deposits: Key factors in their genesis. *Mineralium Deposita* **34**, 227-240.

O'Neill, H.S.C. and Mavrogenes, J.A. 2002. The Sulfide Capacity and the Sulfur Content at Sulfide Saturation of Silicate Melts at 1400°C and 1 bar. *Journal of Petrology* **43**, 1049–1087.

Pagé, P. and Barnes, S.J. 2016. The influence of chromite on osmium, iridium, ruthenium and rhodium distribution during early magmatic processes. *Chemical Geology* **420**, 51-68.

Park, J.W., Hu, Z., Gao, S., Campbell, I.H., and Gong, H. 2012a. Platinum group element abundances in the upper continental crust revisited – New constraints from analyses of Chinese loess. *Geochimica et Cosmochimica Acta* **93**, 63–76.

Park, J.W., Campbell, I.H., and Eggins, S.M. 2012b. Enrichment of Rh, Ru, Ir and Os in Cr spinels from oxidized magmas: Evidence from the Ambae volcano, Vanuatu. *Geochimica et Cosmochimica Acta* **78**, 28–50.

Park. J.W., Campbell, I.H., and Arculus, R.J. 2013a. Platinum-alloy and sulfur saturation in an arc-related basalt to rhyolite suite: Evidence from the Pual Ridge lavas, the Eastern Manus Basin. *Geochimica et Cosmochimica Acta* **101**, 76–95.

Park, J.W., Campbell, I.H., Ickert, R.B., and Allen, C.M. 2013b. Chalcophile element geochemistry of the Boggy Plain zoned pluton, southeastern Australia: a S-saturated barren compositionally diverse magmatic system. *Contributions to Mineralogy and Petrology* **165**, 217–236.

Park, J.W., Campbell, I.H., and Kim, J. 2016. Abundances of platinum group elements in native sulfur condensates from the Niuatahi-Motutahi submarine volcano, Tonga rear arc: Implications for PGE mineralization in porphyry deposits. *Geochimica et Cosmochimica Acta* **174**, 236–246.

Park, J.W., Kamenetsky, V., Campbell, I.H., Park, G., Hanski, E. and Pushkarev, E. 2017. Empirical constrains on partitioning of platinum-group and trace elements in Cr-spinel from primitive terrestrial magmas. *Geochimica et Cosmochimica Acta* **216**, 393–416.

Parkinson, J.J., and Arculus, R.J. 1999. The redox state of subduction zones: insights from arc-peridotites. *Chemical Geology* **160**, 409–423.

Peucker-Ehrenbrink, B., Bach, W., Hart, S.R., Blusztajn, J.S., and Abbruzzese, T. 2003. Rhenium-osmium isotope systematics and platinum group element concentrations in oceanic crust from DSDP/ODP Sites 504 and 417/418. *Geochemistry, Geophysics, Geosystems* **4**, 8911.

Rehkämper, M., Halliday, A.N., Fitton, J.G., Lee, D.C., Wieneke, M., and Arndt, N.T. 1999. Ir, Ru, Pt, and Pd in basalts and komatiites: new constraints for the geochemical behaviour of the platinum-group elements in the mantle. *Geochimica et Cosmochimica Acta* **63**, 3915–3934.

Righter, K., Chesley, J., Geist, D., and Ruiz, J. 1998. Behavior of Re during magma fractionation: an example from Volcan Alcedo, Galapagos. *Journal of Petrology* **39**, 785–795.

Righter, K., Campbell, A., Humayun, M., and Hervig, R. 2004. Partitioning of Ru, Rh, Pd, Re, Ir, and Au between Cr-bearing spinel, olivine, pyroxene and silicate melts. *Geochimica et Cosmochimica Acta* **68**, 867–880.

Ripley, E.M., Brophy, J.G., and Li, C. 2002. Copper solubility in a basaltic melt and sulfide liquid/silicate melt partition coefficients of Cu and Fe. *Geochimica et Cosmochimica Acta* **66**, 2791–2800.

Rudnick, R.L., and Fountain, D.M. 1995. Nature and composition of the continental crust: A lower crustal perspective. *Reviews of Geophysics* **33**, 267–309.

Setiabudi, B.T. 2001. *Geochemistry and Geochronology of the Igneous Suite Associated with the Kelian Epithermal Gold Deposit, Indonesia* (doctoral dissertation). Australian National University, Canberra, Australia.

Shinohara, H. and Hedenquist, J.W., 1997. Constraints on magma degassing beneath the Far Southeast porphyry Cu–Au deposit, Philippines. *Journal of Petrology* **38**, 1741-1752.

Simon, A.C., and Pettke, T. 2009. Platinum solubility and partitioning in a felsic melt–vapor–brine assemblage. *Geochimica et Cosmochimica Acta* **73**, 438–454.

Squire, R. 2001. The volcanological and tectono-magmatic evolution of the Cadia-Neville region, Lachlan Fold Belt, NSW (doctoral dissertation). University of Tasmania, Hobart.

Squire, R., and Crawford, A. 2007. Magmatic characteristics and geochronology of Ordovician igneous rocks from the Cadia–Neville region, New South Wales: implications for tectonic evolution. *Australian Journal of Earth Sciences* **54**, 293–314.

Sun, S.S., and McDonough, W. 1989. Chemical and isotopic systematics of oceanic basalts: implications for mantle composition and processes. *Geological Society, London, Special Publications* **42**, 313–345.

Tagirov, B.R., Baranova, N.N., Zotov, A.V., Akinfiev, N.N., Polotnyanko, N.A., Shikina, N.D., Koroleva, L.A., Shvarov, Y.V., and Bastrakov, E.N. 2013. The speciation and transport of palladium in hydrothermal fluids: Experimental modelling and thermodynamic constraints. *Geochimica et Cosmochimica Acta* **117**, 348–373.

Takamasa, A., and Nakai, S. 2009. Contamination introduced during rock sample powdering: Effects from different mill materials on trace element contamination. *Geochemical Journal* **43**, 389–394.

Tarkian, M., and Koopman, G. 1995. Platinum-group minerals in the Santo Tomas II (Philex) porphyry copper-gold deposit, Luzon Island, Philippines. *Mineralium Deposita*, **30**, 39-47.

Tarkian, M., and Stribrny, B. 1999. Platinum-group elements in porphyry copper deposits: a reconnaissance study. *Mineralogy and Petrology* **65**, 161–183.

Ulrich, T., Gunther, D., and Heinrich, C.A. 1999. Gold concentrations of magmatic brines and the metal budget of porphyry copper deposits. *Nature* **399**, 676–679.

Velasco, F., Tornos, F., and Hanchar, J.M. 2016. Immiscible iron-and silica-rich melts and magnetite geochemistry at the El Laco volcano (northern Chile): Evidence for a magmatic origin for the magnetite deposits. *Ore Geology Reviews* **79,** 346-366.

Wilson, A.J., Cooke, D.R., Stein, H.J. Fanning, C.M., Holliday, J.R., and Tedder, I.J. 2007. U-Pb and Re-Os geochronologic evidence for two alkalic oorphyry ore-forming events in the Cadia District, New South Wales, Australia. *Economic Geology* **102**, 3–26.

Wolf, R., and Anders, E. 1980. Moon and Earth: compositional differences inferred from siderophiles, volatiles, and alkalis in basalts. *Geochimica et Cosmochimica Acta* **44**, 2111–2124.

Wyborn, D., and Sun, S. 1993. Nd-isotopic 'fingerprinting'of Cu/Au mineralisation in the Lachlan Fold Belt. *AGSO Research Newsletter* **19**, 13–14.

Yang, X.M. 2012. Sulphur solubility in felsic magmas: implications for genesis of intrusion-related Gold Mineralization. *Geoscience Canada* **39**.

Yang, A.Y., Zhou, M.F., Zhao, T.P., Deng, X.G., Qi, L., and Xu, J.F. 2014. Chalcophile elemental compositions of MORBs from the ultraslow-spreading Southwest Indian Ridge and controls of lithospheric structure on S-saturated differentiation. *Chemical Geology* **382**, 1–13.

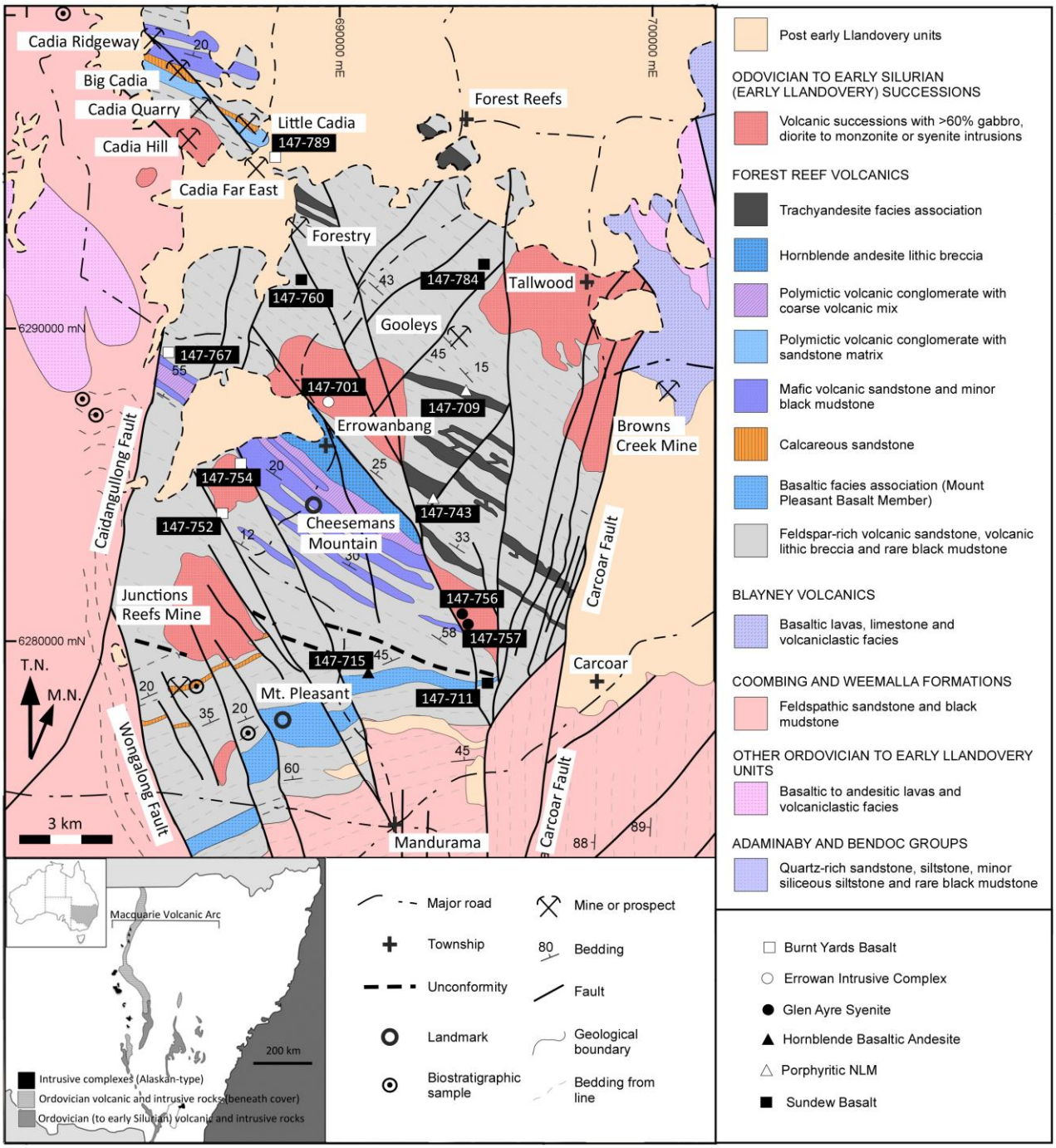

Fig. 1 Geological map of the Cadia-Neville study region showing the approximate location of samples used in this study. Note that sample 147-789 was collected from drillcore and does not sample Tertiary Basalts (Post early Llandovery Units) as depicted on the map. Main map modified from Squire and Crawford (2007) and inset map modified from Cooke et al. (2007).

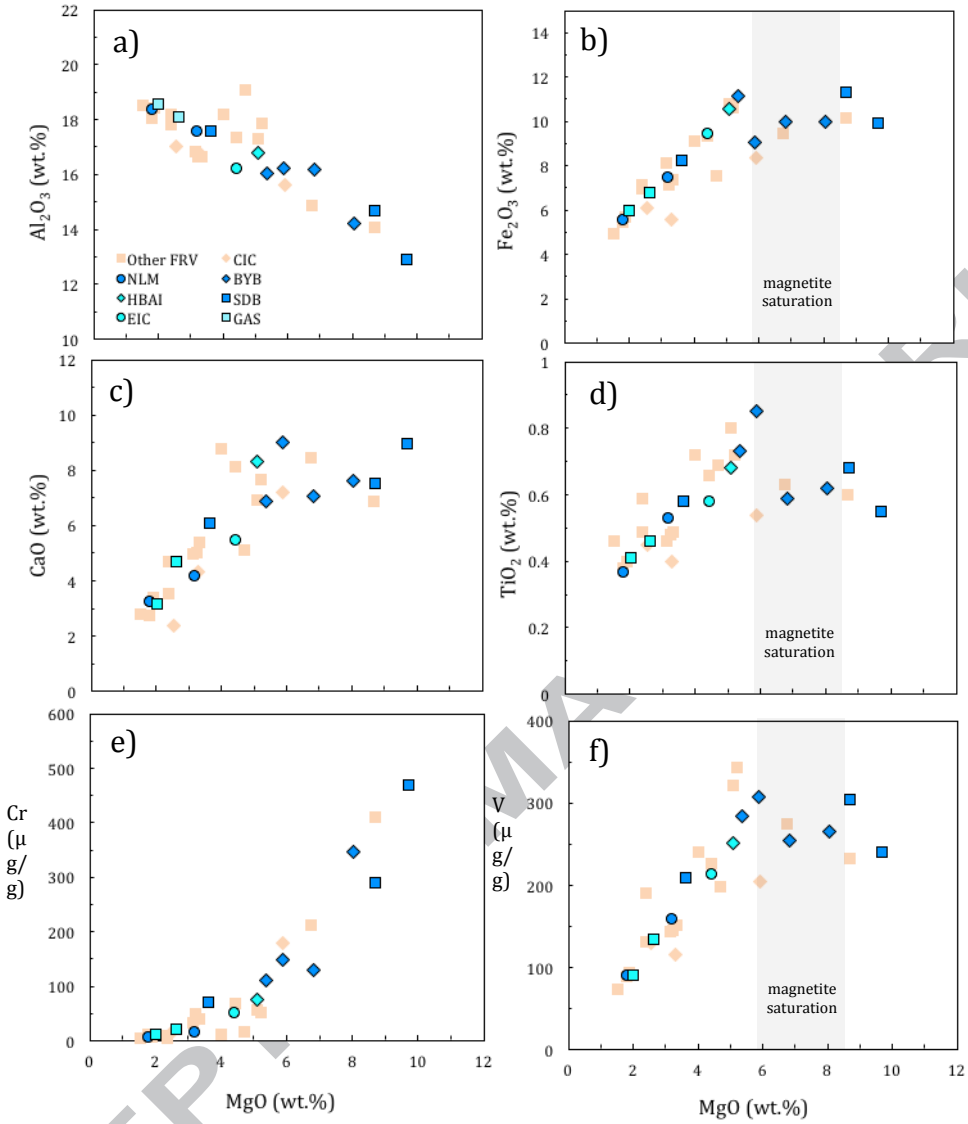

Fig. 2 (a-f) Whole rock major, minor and trace element co-variations plotted against MgO for samples from the Forest Reef Volcanics (FRV). Symbols in blue represent samples used in this study. Dark blue symbols = volcanics; light blue symbols = intrusive rocks; orange diamonds = Cadia Intrusive Complex (CIC); orange squares = other Forest Reef Volcanic samples not used in this study. Major and trace element data, measured by XRF and ICP-MS, from Squire (2001) and Squire and Crawford (2007). BYB = Burnt Yards Basalt; EIC = Errowan Intrusive Complex; GAS = Glen Ayre Syenite; HBAI = Hornblende Basalt Andesite Intrusive; NLM = Nullawonga Latite Member; SDB = Sundew Basalt. Note. Scatter in the data, particularly CaO, is, in part, attributed to weak hydrothermal alteration and multiple magma injections following replenishment.

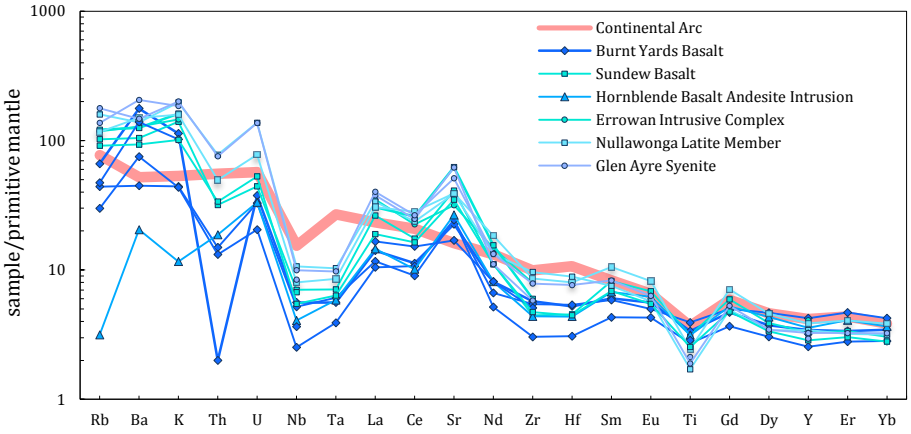

Fig. 3 Primitive mantle-normalised spidergram showing the trace element pattern of Forest Reef Volcanic samples used in this study. The trace element signature of typical continental arc is show for comparison. Continental arc values from Rudnick and Fountain (1995) and primitive mantle values taken from Sun and McDonough (1989). Trace elements measured by XRF and ICP-MS, from Squire (2001) and Squire and Crawford (2007).

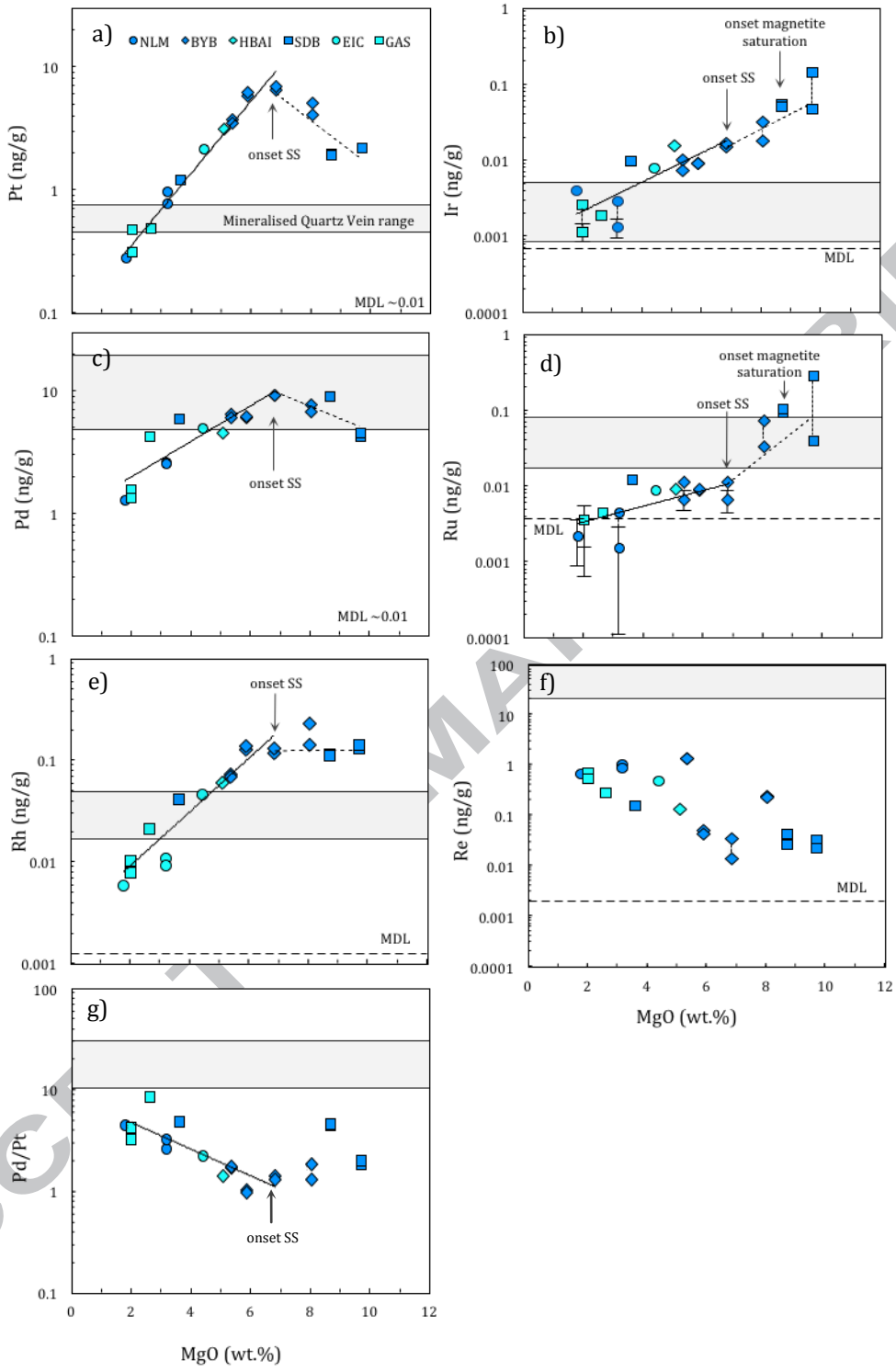

Fig. 4 (a-g) Whole-rock PGE and Re concentrations plotted against MgO for the Forest Reef Volcanics depicting the point of sulfide saturation (SS). Dark blue symbols = volcanics; light blue symbols = intrusive rocks. BYB = Burnt Yards Basalt; EIC = Errowan Intrusive Complex; GAS = Glen Ayre Syenite; HBAI = Hornblende Basalt Andesite Intrusive; NLM = Nullawonga Latite Member; SDB = Sundew Basalt. Grey areas denote minimum and maximum PGE concentrations in the two mineralised quartz veins. Vertical dashed lines connect duplicate analyses. Trend lines are nonlinear exponential least squares fit for the high-Mg (dashed) and low-Mg samples (solid). Analytical uncertainties (2σ), large enough for display, are shown. Where method detection limits (MDL) are too small to display their values are provided. MgO data from Squire (2001).

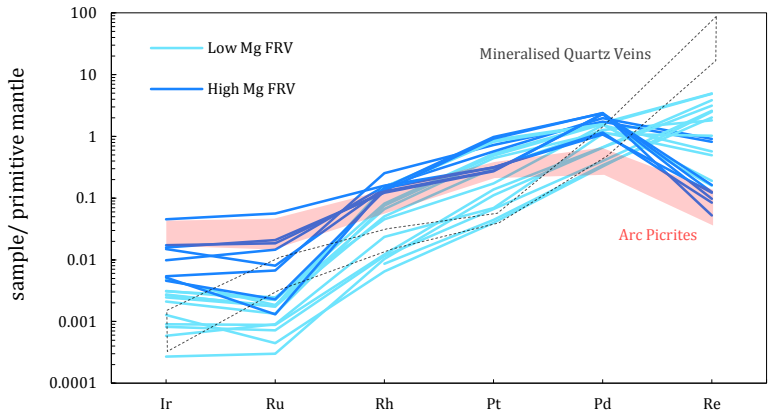

Fig. 5 Primitive mantle-normalised PGE and Re concentrations of the high-Mg and low-Mg samples from the Forest Reef Volcanics. The PGE and Re range of two mineralised quartz veins from Cadia (grey dashed; this study) and arc picrites (purple; >10 wt.% MgO) are shown for comparison. Arc picrite data from Woodland et al. (2002). Primitive mantle PGE and Re concentrations from McDonough and Sun (1995).

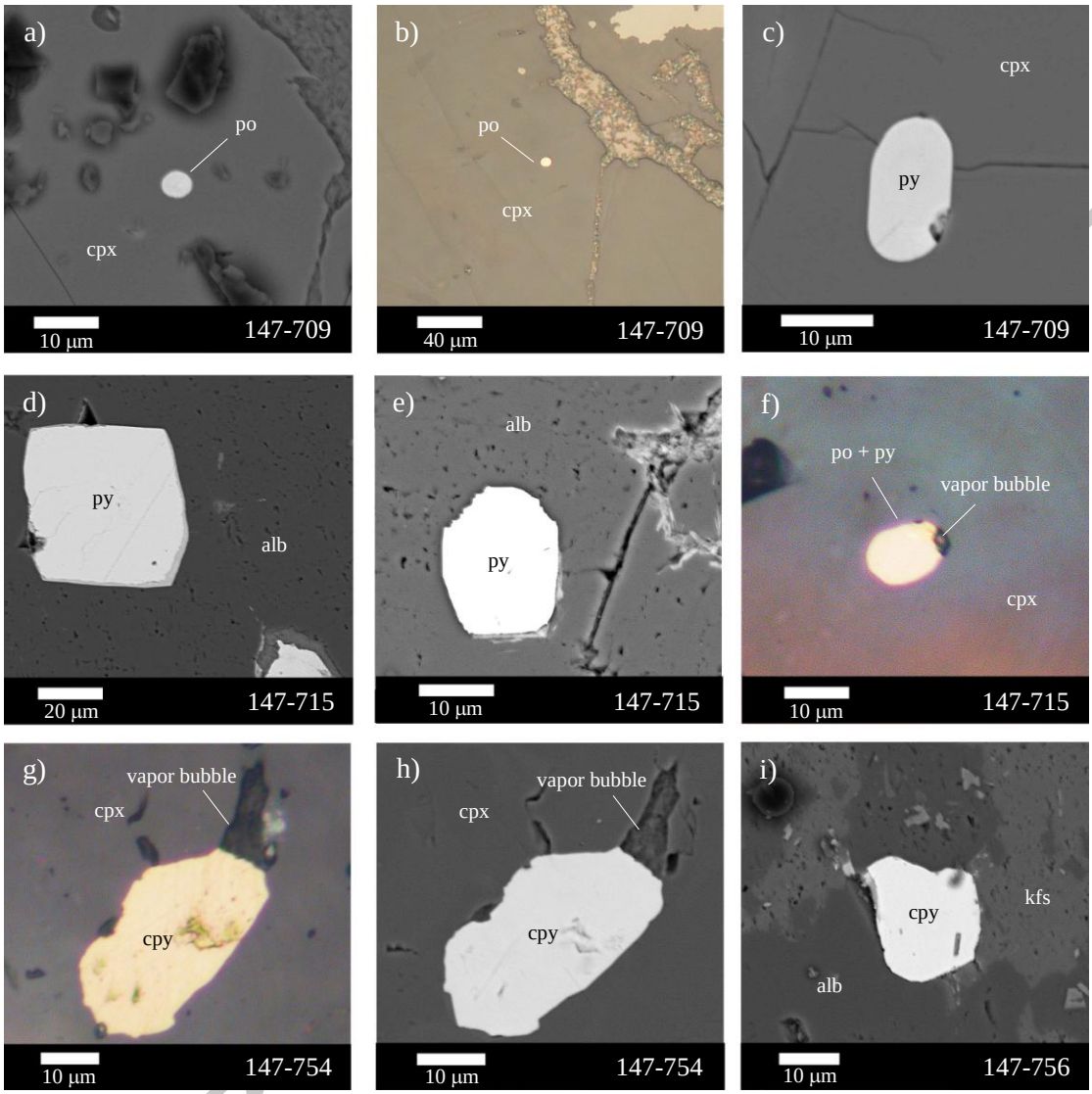

Fig. 6 (a-i) SEM and optical microscope images of magmatic sulfide melt inclusions found in low-Mg samples from the Forest Reef Volcanics, which contain ≤6.8 wt.% MgO. (a,b) Round pyrrhotite in cumulus clinopyroxene in porphyritic trachyandesite (147-709). (c) round pyrite in cumulus clinopyroxene in porphyritic trachyandesite (147-709). (d) cubic pyrite in sieve-textured plagioclase phenocryst in porphyritic basaltic andesite (147-715). (e) subhedral pyrite trapped in sieve-textured plagioclase phenocryst in porphyritic basaltic andesite (147-715). (f) rounded pyrrhotite and pyrite sulfide bleb trapped along with vapor bubble in cumulate clinopyroxene in in porphyritic basaltic andesite (147-715). (g,h) Cu-rich sulfide and vapor bubble trapped in cumulate clinopyroxene in basalt (146-754). (i) Cu-rich sulfide trapped in sieve-textured K-feldspar phenocryst that is partially replaced by albite in a holocrystalline syenite (147-756). *Alb* = albite; *cpy* = chalcopyrite; *cpx* = clinopyroxene, kfs = K-feldspar; *po* = pyrrhotite; *py* = pyrite. Note. Pyrite and pyrrhotite are interpreted to have crystallised after sulfide melt inclusions were trapped.

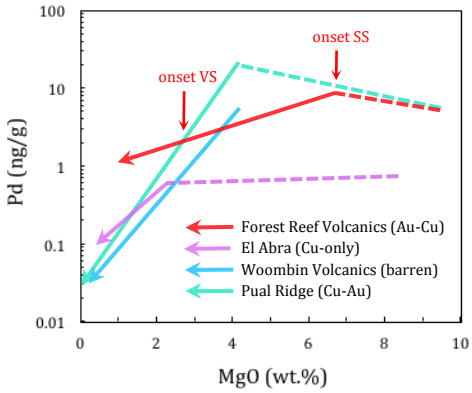

Fig. 7 A plot comparing the rate of Pd depletion with decreasing MgO, following sulfide saturation, in Forest Reef Volcanics (i.e. Cadia; Au-Cu deposit), the El Abra-Pajonal Intrusive suite (Cu-only deposit; Cocker et al., 2016), Woombin suite (barren; Hao et al., 2017) and Pual Ridge (Cu-Au; Park et al., 2013a). Dashed lines = pre-sulfide saturation, and solid lines = post-sulfide saturation. The rate of Pd depletion in the Forest Reef Volcanics is appreciably less than for any of the other sulfide saturated systems, which is attributed to either a lower fraction of sulfide melt and/or a smaller *effective* R factor in the former, relative to the latter.

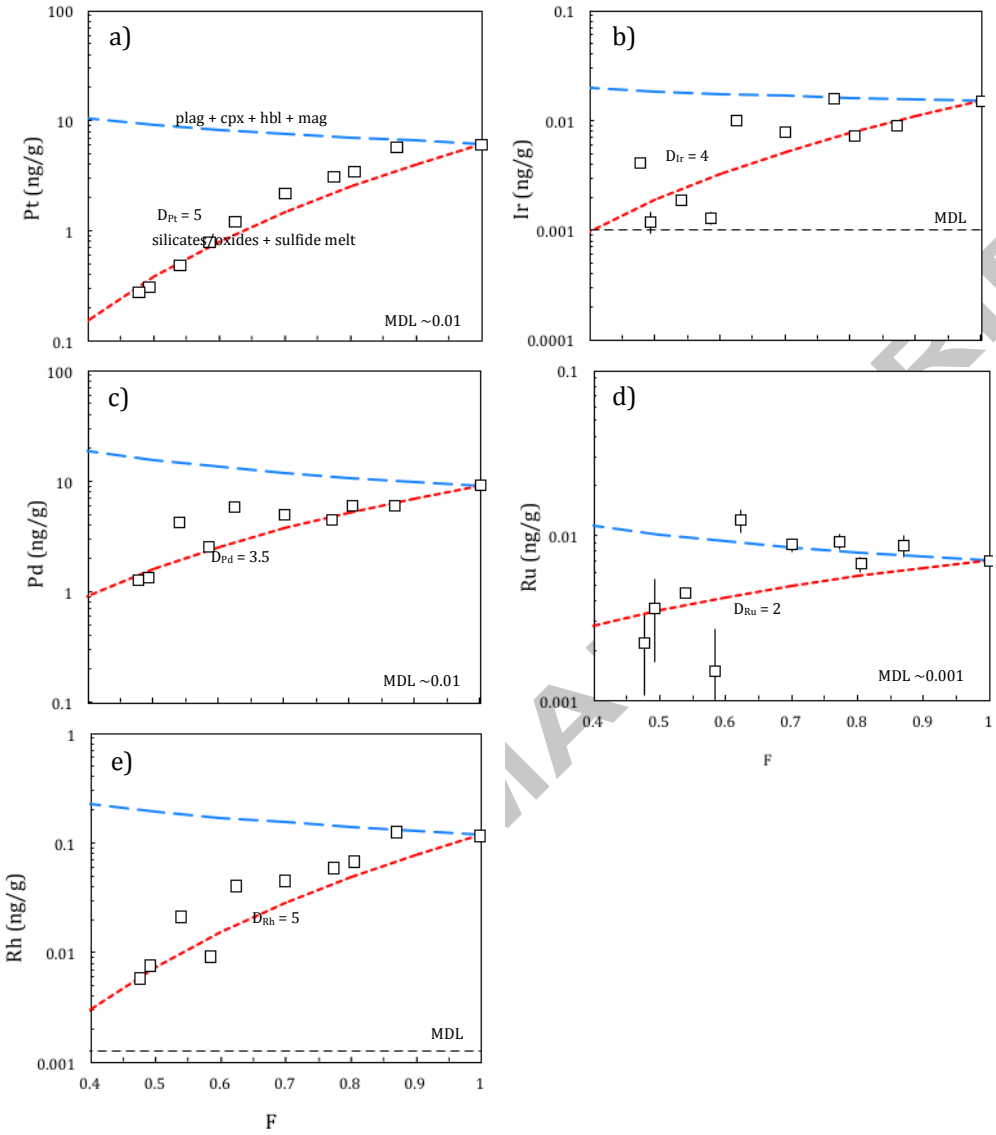

Fig. 8 (a-e) Co-variation plots of PGE in the low-Mg samples modeled as a function of *fraction melt remaining* (F), assuming F=1 at 6.8 wt.% MgO. The fractionation factor was calculated using Zr. The fractionation of PGE was then modeled for 1) the fractionation of a simple silicate and oxide assemblage represented in blue (plag:cpx:hbl:mag = 60:29:10:1) and 2) silicate and oxide assemblage containing sulfide melt. The rate of PGE depletion can be explained by the saturation of either (i) 0.003 wt.% sulfide melt, assuming complete equilibrium between the sulfide and silicate melt, such that $D_{Pd}^{sul} \sim 10^5$, or (ii) 0.023 wt.% sulfide melt, assuming limited equilibrium between the sulfide and silicate melt, such that $D'_{Pd}{}^{sul} \sim 10^4$. Note, only the lowest data points from duplicate analyses have been plotted.

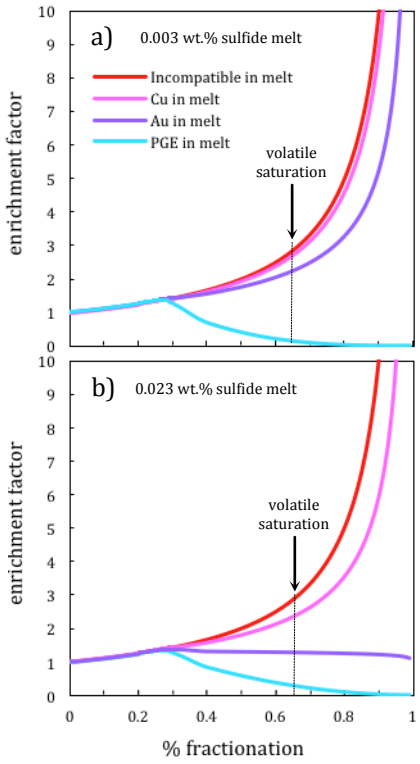

Fig. 9 (a,b) Model simulating the PGE, Cu and Au concentration of the silicate melt, as a function of fractional crystallisation, following a) 0.003 wt. % sulfide melt precipitation with an infinite R factor and, b) 0.023 wt.% sulfide melt precipitation with a smaller R factor of 1.4 x 10^4. The silicate melt begins to precipitate a sulfide melt after ~34% fractionation (F calculated from the increase in Zr in the high-Mg rocks). Volatile saturation is estimated to have occurred following ~65% crystal fractionation however its affects on PGE, Cu or Au concentrations are not shown to demonstrate how further crystal fractionation would enrich the magma in these elements. See text for further details.

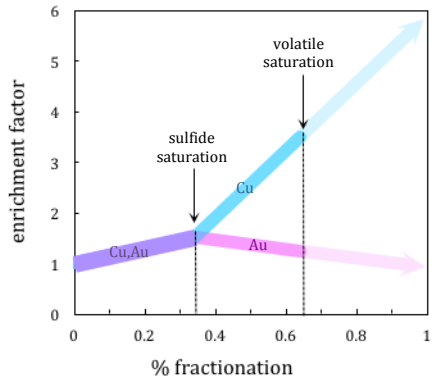

Fig. 10 A schematic diagram showing the enrichment of Cu and Au in the Forest Reef magma with fractional crystallisation following the saturation of 0.023 wt.% sulfide melt (onset at 6.8 wt.% MgO) up to the point of volatile saturation (at 2.9 wt.% MgO). The net enrichment of Cu and Au in the silicate melt from 9.8 to 2.9 wt.% MgO is x3.5 and x1.24, respectively. Precipitation of 0.023 wt.% sulfide melt would have depleted Au by only 18% from the time of sulfide saturation to the time of volatile saturation.

Table 1. Whole rock concentrations of MgO, PGE and Re in samples from the Forest Reef Volcanics.

Sample	MgO[a] (wt.%)	Ir (pg/g)	Ru (pg/g)	Rh (pg/g)	Pt (pg/g)	Pd (pg/g)	Re (pg/g)
Sundew Basalt							
147-784[1]	9.7	48 ± 3	40 ± 3	129 ± 3	2217 ± 77	4206 ± 169	34 ± 4
147-784 D[3]	9.7	146 ± 6	282 ± 14	143 ± 7	2220 ± 57	4509 ± 227	24 ± 4
RD (%)		204	605	11	0.1	7	-29
147-760[1]	8.7	55 ± 3	92 ± 8	115 ± 2	1985 ± 66	9011 ± 310	46 ± 4
147-760 D[2]	8.7	51 ± 3	104 ± 16	110 ± 17	1928 ± 65	8978 ± 1239	27 ± 5
RD (%)		-7	13	-4	-3	-0.4	-41
Burnt Yards Basalt							
147-767[2]	8.0	18 ± 2	34 ± 4	227 ± 9	5132 ± 317	6772 ± 329	229 ± 13
147-767 D[3]	8.0	32 ± 2	73 ± 10	140 ± 4	4059 ± 183	7677 ± 318	254 ± 22
RD (%)		78	115	-38	-21	13	11
147-754[2]	6.8	17 ± 1	7 ± 2	131 ± 4	6939 ± 227	9166 ± 522	15 ± 4
147-754 D[3]	6.8	15 ± 1	11 ± 1	118 ± 6	6539 ± 288	9317 ± 536	35 ± 4
RD (%)		-12	57	-10	-6	2	133
147-789[2]	5.9	9.0 ± 0.5	9.0 ± 1.9	136 ± 6	6224 ± 469	6133 ± 446	44 ± 5
147-789 D[3]	5.9	9.2 ± 0.8	8.7 ± 1.5	127 ± 4	5814 ± 149	6032 ± 321	53 ± 6
RD (%)		2	-3	-7	-7	-2	20
147-752[1]	5.4	10.1 ± 0.8	11.2 ± 1.0	73 ± 2	3742 ± 109	6463 ± 296	1394 ± 54
147-752 D[2]	5.4	7.3 ± 0.7	6.7 ± 2.1	68 ±3	3488 ± 231	6124 ± 328	1377 ± 81
RD (%)		-28	-40	-7	-7	-5	-1
Hornblende Basalt Andesite Intrusion							
147-715[2]	5.1	15.9 ± 0.5	9.2 ± 1.3	60 ± 2	3135 ± 156	4551 ± 251	138 ± 8
Errowan Intrusive Complex							
147-701[1]	4.4	7.8 ± 0.7	8.8 ± 1.1	46 ± 2	2176 ± 61	4980 ± 331	509 ± 19
Sundew Basalt							
147-711[1]	3.6	9.9 ± 0.4	12.4 ± 2.3	41 ± 1	1224 ± 32	5950 ± 141	159 ± 6
Porphyritic Nullawonga Latite Member							
147-709[1]	3.2	2.9 ± 0.4	4.4 ± 1.0	10.9 ± 0.7	979 ± 41	2585 ± 131	1075 ± 57
147-709 D[2]	3.2	1.3 ± 0.4	<3.7	9.3 ± 0.7	785 ± 45	2579 ± 189	879 ± 58
RD (%)		-55		-15	-20	0	-18
Glen Ayre Syenite							
147-756[1]	2.6	1.9 ± 0.2	4.5 ± 0.8	21.3 ± 0.8	490 ± 15	4293 ± 129	286 ± 8
147-757[1]	2.0	2.6 ± 0.3	<3.6	10.4 ± 0.4	474 ± 14	1559 ± 61	729 ± 28
147-757 D[2]	2.0	1.2 ± 0.3	<3.7	7.7 ± 0.3	313 ± 17	1338 ± 66	567 ± 31
RD (%)		-54		-26	-34	-14	-22
Porphyritic Nullawonga Latite Member							
147-743[1]	1.8	4.1 ± 0.3	2.2 ± 1.3	5.8 ± 0.6	282 ± 9	1271 ± 35	699 ± 35
Quartz-sulfide vein							
SV-E[2]	N.D.	3.7 ± 0.3	60 ± 12	50 ± 13	547 ± 21	14 380 ± 2526	147 857 ± 7785
SV-E D[3]	N.D	2.4 ± 0.2	80 ± 8	24 ± 4	461 ± 15	4871 ± 438	97 713 ± 4402
RD (%)		-35	33	-52	-16	34693	-34
SV-L [2]	N.D.	5.2 ± 0.4	19 ± 2	17 ± 4	574 ± 19	17 799 ± 1180	33 173 ± 2416
SV-L D[3]	N.D	0.9 ± 0.1	17 ± 5	20 ± 5	758 ± 35	19 758 ± 2267	20 745 ± 1012
RD (%)		-83	-11	18	32	12	-39

Notes

[1] samples processed in batch 1
[2] samples processed in batch 2
[3] samples processed in batch 3
[a] Squire (2001)
MQV-E = Early-stage mineralised quartz vein
MQV-L = Late-stage mineralised quartz vein
RD = relative difference

Italics denotes analyses with interference corrections >50%
Uncertainties have been quoted as 2σ
N.D. = No data
D = Duplicate
Ir, Rh, Pt, Re from batch 2 and 3 samples corrected using 3 blank average and Ru and Pd using 4 blank average.